Materials Today Bio 12 (2021) 100154

Contents lists available at ScienceDirect

Materials Today Bio

journal homepage: www.journals.elsevier.com/materials-today-bio

Localized disruption of redox homeostasis boosting ferroptosis of tumor by hydrogel delivery system

Xiaomin Su [a,b,1], Yongbin Cao [c,1], Yao Liu [d], Boshu Ouyang [e,g], Bo Ning [a], Yang Wang [a], Huishu Guo [a,**], Zhiqing Pang [f,***], Shun Shen [b,*]

[a] Central Laboratory, First Affiliated Hospital, Institute (College) of Integrative Medicine, Dalian Medical University, Dalian, 116021, China
[b] Center for Medical Research and Innovation, Shanghai Pudong Hospital, Fudan University Pudong Medical Center, Shanghai, 201399, China
[c] Zhuhai Precision Medical Center, Zhuhai People's Hospital (Zhuhai Hospital Affiliated with Jinan University), Zhuhai, 519000, Guangdong, PR China
[d] The Institute for Translational Nanomedicine, Shanghai East Hospital, Tongji University School of Medicine, Shanghai, 200120, China
[e] Department of Integrative Medicine, Huashan Hospital, Fudan University, Shanghai, China
[f] School of Pharmacy & Key Laboratory of Smart Drug Delivery, Fudan University, Shanghai, 201203, China
[g] Institutes of Integrative Medicine, Fudan University, Shanghai, China

ARTICLE INFO

Keywords:
Ferroptosis
Redox homeostasis
Glutathione peroxidase
Alkyl radicals
Hydrogel

ABSTRACT

Ferroptosis has received ever-increasing attention due to its unparalleled mechanism in eliminating resistant tumor cells. Nevertheless, the accumulation of toxic lipid peroxides (LPOs) at the tumor site is limited by the level of lipid oxidation. Herein, by leveraging versatile sodium alginate (ALG) hydrogel, a localized ferroptosis trigger consisting of gambogic acid (GA), 2,2′-azobis [2-(2-imidazolin-2-yl) propane] dihydrochloride (AIPH), and Ink (a photothermal agent), was constructed via simple intratumor injection. Upon 1064 nm laser irradiation, the stored AIPH rapidly decomposed into alkyl radicals (R•), which aggravated LPOs in tumor cells. Meanwhile, GA could inhibit heat shock protein 90 (HSP90) to reduce the heat resistance of tumor cells, and forcefully consume glutathione (GSH) to weaken the antioxidant capacity of cells. Systematic in vitro and in vivo experiments have demonstrated that synchronous consumption of GSH and increased reactive oxygen species (ROS) facilitated reduced expression of glutathione peroxidase 4 (GPX4), which further contributed to disruption of intracellular redox homeostasis and ultimately boosted ferroptosis. This all-in-one strategy has a highly effective tumor suppression effect by depleting and generating fatal active compounds at tumor sites, which would pave a new route for the controllable, accurate, and coordinated tumor treatments.

1. Introduction

Ferroptosis, marked by the accumulation of iron-dependent LPOs, is another intriguing form of programmed cell necrosis discovered in recent years [1–3]. Unlike traditional programmed cell death, ferroptosis is expected to be a promising treatment for cancer due to the independence of point apoptosis-related proteins [4,5]. Previous research has shown that aggravation of cell-member LPOs was highly dependent on the reaction of Fe^{2+} with H_2O_2 in the tumor to generate hydroxyl free radicals. While, the Fenton reaction is limited by the undesirable tumor microenvironment, such as the unsuitable pH [6,7], H_2O_2 level [8], and high expression of antioxidants (such as GSH) [9,10], which negatively influences the therapeutic effect. Fortunately, inhibiting glutathione peroxidase (GPX4), a critical metabolic enzyme that detoxifies LPOs,

Abbreviations: LPO, lipid peroxides; ALG, sodium alginate; CLSM, confocal laser scanning microscope; DMEM, Dulbecco's Modified Eagle's Medium; DAPI, 4′,6-diamidino-2-phenylindole; DLS, dynamic light scattering; GA, gambogic acid; AIPH, 2,2′-azobis [2-(2-imidazolin-2-yl) propane] dihydrochloride; FBS, fetal bovine serum; R•, alkyl radicals; GSH, glutathione; HE, hematoxylin eosin; HSP90, heat shock protein 90; IR, inhibitory rate; GPX4, glutathione peroxidase 4; ROS, reactive oxygen species; NPs, nanodrugs; PTT, photothermal therapy; CCK–8, Cell counting kit-8; ABTS, 2,2-Azobis (3-ethylbenzothiazoline-6-sulfonic acid); DCFH-DA, 2,7-dichlorofluorescin diacetate; DTNB, 5,5′-Dithiobis-(2-nitrobenzoic acid); Fer-1, Ferrostatin -1; DFO, deferoxamine mesylate.

* Corresponding author.
** Corresponding author.
*** Corresponding author.
E-mail addresses: guohuishu1@126.com (H. Guo), zqpang@fudan.edu.cn (Z. Pang), nanocarries@gmail.com (S. Shen).
[1] These authors contributed equally to this work.

https://doi.org/10.1016/j.mtbio.2021.100154
Received 23 August 2021; Received in revised form 21 October 2021; Accepted 30 October 2021
Available online 2 November 2021

reportedly also promotes ferroptosis in cancer cells. Hence, various strategies to inactivate GPX4, especially the use of GSH scavengers, such as erastin [11,12], and L-buthionine sulfoximine [13–15], have attracted widespread interest. Although these agents have shown potential in ferroptosis-induced cancer therapy, their therapeutic efficiency still remains to be enhanced because of the abundant supply of GSH from the rapid proliferation of tumor tissue [16]. Therefore, decreasing the antioxidant capacity of tumor cells together with triggering oxidative stress to completely block redox homeostasis and aggravate LPOs accumulation may be critical to the success of tumor ferroptosis therapy.

Redox homeostasis refers to the equilibrium between the production and elimination of ROS, which plays a unique role in the process of ferroptosis [17] and could protect cancer cells from oxidative stress and promote cell proliferation and tumor growth. Therefore, upsetting the redox balance is a promising strategy for cancer treatment. However, previous studies have focused on reducing the antioxidant capacity [18,19] or increased oxidative stress [20] unilaterally. The increase in oxidative stress mainly depends on a singlet oxygen, hydroxyl radicals, or peroxides produced by various strategies. However, cancer cells have evolved a powerful antioxidant system, of which GSH is a characteristic antioxidant, to counter oxidative stress. The main processes of GSH consumption are the oxidation of GSH [21,22], hindrance of GSH composites [23,24], and the increase of GSH outflow [25]. Intriguingly, GSH consumption is related to ferroptosis. Consumption of GSH will cause inactivation of GPX4, which could catalyze the degradation of hydrogen peroxide and hydroperoxide and inhibit the generation of lipid ROS [26]. Numerous nanomaterials with GSH depletion abilities have been shown to trigger ferroptosis, providing supplementary strategies for inducing ferroptosis [27]. For example, Zhao and his collaborators used electron-accepting micelles to deplete the reduced nicotinamide adenine dinucleotide phosphate and impaired GSH and thioredoxin redox cycle for ferroptosis-induced tumor eradication [28]. Cai and his coworkers used targeted nanosheets with Fe (II) overload and GSH consumption to induce ferroptosis through GSH consumption and abnormal iron metabolism [29]. Nonetheless, a unilateral strategy is far from sufficient to eliminate all tumor cells [30]. To completely break the redox balance for more effective treatment of tumors, strategies to reduce the antioxidant capacity of tumor cells need to be combined with other methods to enhance oxidative stress and LPOs accumulation.

In recent years, the use of cytotoxic free radicals to eliminate tumors has emerged as a treatment strategy. It is well known that the hypoxic tumor microenvironment affects the production of ROS [31]. The compound AIPH has good water solubility and can decompose into alkyl radicals under heat even under anaerobic conditions [32–36]. For instance, Huang et al. loaded AIPH into porous hollow iron-oxide nanoparticles and induced its magnetothermal decomposition [37]. Alternatively, Li and collaborators reported a Bi_2Se_3 nanoparticles that could melt lauric acid under photothermal conditions and promote the release and decomposition of AIPH [36]. Further, in our previous research, we reported that AIPH combined with low-temperature photothermal therapy (PTT) achieved antitumor therapy through lipid peroxidation [33]. We are aware of only a few reports concerning the combination of free radicals and GA to destroy tumors through the ferroptosis pathway with depletion of GSH and aggravation of LPOs accumulation [38].

GA is one of the effective ingredients extracted from the *Garcinia cambogia* tree and has been proven to have excellent and extensive antitumor effects on breast cancer, lung cancer, and gastric cancer, among others, in clinical practice [39–42]. The outstanding therapeutic efficacy can be attributed to the broad-spectrum mechanism of GA that involves, but is not confined to, induction of apoptosis, antiproliferation, and suppression of the NF-κB signaling pathway [42–44]. Moreover, GA has been shown to inhibit HSP90 expression and increase GSH depletion in cancer cells [41,45]. Previous studies have demonstrated that GA mainly targeted TrxR and inhibited the reduction of thioredoxin, which ultimately resulted in ROS generation and the disruption of intracellular redox homeostasis [44,46,47]. For example, Liang and a coworker reported a HA–GA@Ce6 nanoparticle that could deplete intracellular GSH to enhance photodynamic therapy [48]. Furthermore, Lan et al. prepared a new carrier-free GA–Ce6–FA nanoparticles, which induced GA to consume GSH to enhance chemophotodynamic therapy through drug release triggered by a slightly acidic environment [46]. Therefore, GA, whether alone or in combination, is a promising drug for the treatment of tumors.

The study aim was to investigate a simple drug delivery system that induces ferroptosis of tumor cells with the use of an injectable ALG hydrogel to encapsulate GA, AIPH, and Ink (Scheme 1). ALG consists of guluronic and mannuronic acid regions, which could quickly bind to Ca^{2+} in vivo to form the structure of "egg box". One of the main properties of ALG is the formation of an in-situ hydrogel [49–52]. Biocompatible and biodegradable ALG was used as a drug carrier to achieve appropriate controlled release of the drugs in tumor tissues. Compared with other gels, ALG has excellent properties, such as softness, non-toxicity, high water content, and the structure similar to that of the extracellular matrix [53], which has led to its wide use as a drug carrier [50,54], in cell transplants [55,56], and in wound dressing [57,58]. Conventional Chinese Ink, with excellent photothermal performance and superior biocompatibility, was selected as a photothermal agent [59,60]. The AIPH, GA, Ink, and ALG were simply mixed, and a minimally invasive method was used to inject the mixture into the tumor. Upon 1064 nm laser irradiation, the increased temperature in the tumor caused decomposition of AIPH into R• and oxidation of cell membrane lipids. To upset the redox balance, GA was used to consume GSH, which reduces the antioxidant capacity of cells. In addition, GA has also been shown to inhibit HSP90, diminish the heat tolerance of tumor cells, and strengthen the antitumor effect [61–65]. The synergistic effect of GA and AIPH was found to aggravate increased lipid oxidation in cell membranes and to induce ferroptosis. Furthermore, the synchronous consumption of GSH and increase in ROS also facilitated reduced expression of GPX4, which further contributed to the disruption of intracellular redox homeostasis and ultimately induced ferroptosis. With advantages over the single-agent treatment approach, this design exhibits a synergistic effect in the treatment process in vivo and in vitro and is potentially a breakthrough in tumor therapy.

2. Materials and methods

2.1. Materials

GA of 97.0% purity over was supplied by Aladdin Corporation (Aladdin, Shanghai, China). Hu-Ink was the product of Hu Kai wen Ink Factory, China. GPX4 and HSP90 antibodies were the products of Abcam (Shanghai, China). AIPH, sodium alginate, and Calcium chloride were purchased from Aladdin Company (Shanghai, China). Cell counting kit-8 (CCK–8), Live and Dead Dye Kit, 4′,6-Diamidino-2-phenylindole (DAPI) were provided by Key Gen Bio-Tech (Nanjing, China). 2,2-Azobis (3-ethylbenzothiazoline-6-sulfonic acid) (ABTS), 2,7-dichlorofluorescin diacetate (DCFH-DA) were obtained from Sigma-Aldrich. BCA protein assay kit was provided by Multisciences (Nanjing, China). Dulbecco's modified Eagle's medium were purchased from GE Healthcare Life Science. The concentration of GSH in the cell was detected by 5,5′-Dithiobis-(2-nitrobenzoic acid) (DTNB) Macklin (Shanghai, China). Life Science (Gibco, Pittsburgh, USA) provided fetal bovine serum and trypsin−EDTA. Nude mice were provided by Shanghai SLAC Lab Animal Co. Ltd. TUNEL assay apoptosis detection kit was purchased from absin (Shanghai, China).

2.2. Construction and characterization of hydrogels

Firstly, the enrichment of Ink was diluted with distilled water to get lower concentrations, which could be stored for further experiment. Malvern Zetasizer ZS90 device was exploited to measured z-average

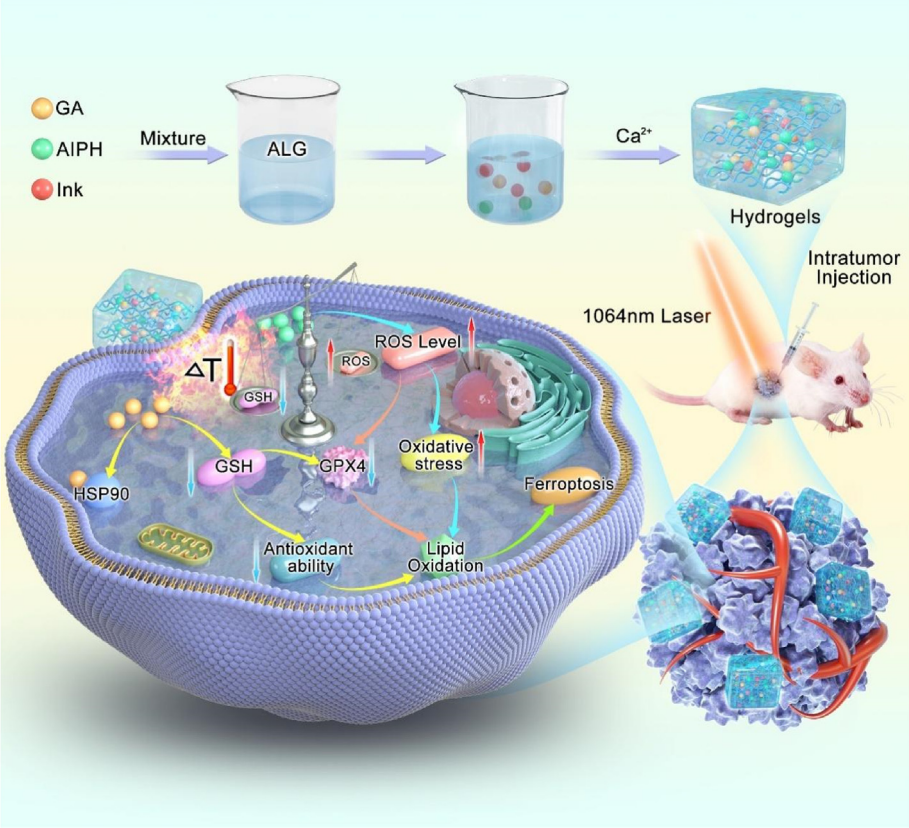

Scheme 1. Schematic diagram of the mechanism of GA–AIPH–Ink–ALG inducing ferroptosis.

diameter and zeta potentials of Ink. ALG, Ink, AIPH, and GA were simply mixed to obtain an injectable ALG–Ink–AIPH–GA cocktail. Owing to the invariable concentration of Ca2+ in vivo, it is necessary to select the appropriate concentration of ALG mixed solution. The property of ALG hydrogel is related to concentration. To confirm the hydrogel performance of ALG, Ink (1 mg/mL) and increasing concentrations of ALG (1, 5, 10, and 20 mg/mL) were mixed in a small beaker. Subsequently, the mixture was injected into the solution containing 1.8 mmol/L Ca^{2+}. At the same time, separate Ink or ALG–Ink mixed solution containing 5 mg/mL ALG was contrasted by the same method, and pictures were taken at different times. A scanning electron microscope (SEM) was used to visually observe the appearance of ALG–Ink–AIPH–GA. The drug release from the ALG–Ink–AIPH–GA hydrogel was detected by spectrophotometer (PerkinElmer Lambda 750). 100 μL of ALG (5 mg/mL) mingled with Ink (1 mg/mL) or AIPH (200 μg/mL) or GA (200 μg/mL) were breathed into 4 mL Ca^{2+} solution, and they were wobbled on a constant temperature shaker for 24 h at 37 °C. The UV–Vis–NIR spectrophotometer was employed to detect the absorption spectrum of the supernatant and the photographs were taken by mobile phone.

2.3. Photothermal effects measurements

To investigate the photothermal performance of the mixed solution, different groups of H_2O, ALG, Ink, GA, ALG–Ink, ALG–Ink–AIPH, and ALG–Ink–AIPH–GA were irradiated with a 1064 nm laser (0.5W/cm^2) for 10 min. Near-infrared imager was applied to record temperature changes. Subsequently, the photothermal performance of Ink at diverse concentrations were monitored by the method mentioned above. Finally, the photothermal stability of Ink and gel composites was also explored through a near-infrared equipment.

2.4. Detection of free radicals

The formation of free radical was detected by the principle that ABTS could capture free radical to form $ABTS^{+\bullet}$. The AIPH (200 μg/mL, 0.2 mL) was mixed with ABTS liquid (2 mg/mL, 0.2 mL). The mixture was avoided from laser illumination and subjected to reaction in 37 °C or 44 °C water bath for 2, 4, and 6 h, respectively. The absorbance of $ABTS^{+\bullet}$ solution ranging from 400 to 900 nm was measured with a UV-Vis spectrophotometer.

To detect the formation of $ABTS^{+\bullet}$ under laser irradiation, ABTS aqueous solution (2 mg/mL, 0.2 mL) and ALG–Ink–AIPH–GA aqueous solution (2 mg/mL, 0.2 mL) were mixed in a test tube, and the solution was illuminated with a 1064 nm laser (0.5W/cm^2) for different times. The UV-Vis spectrophotometer was used to record the absorbance of the liquor from 400 to 900 nm at diverse time points. The automatic microplate spectrophotometer was employed to note the absorbance curve of different groups of diluted solution at 736 nm with different irradiation times.

2.5. Detection of free radicals in cells

The formation of free radicals was detected by DCFH-DA in cells. HCT116 cells were hatched with different concentrations of AIPH (60 μg/mL), Ink (25 μg/mL), ALG (1 mg/mL), GA (1 μg/mL), with or without 1064 nm laser irradiation (0.5 W/cm^2, 10 min), and incubated for another 6 h. Then, the cells were cleansed with PBS two times, and hatched with DCFH-DA (20 μM) for 25 min. Finally, the supernatant solution was removed and the nuclei were labeled with DAPI for 10 min in the dark. CLSM or flow cytometry was applied to observe the fluorescence of DCF.

2.6. In vitro synergistic cytotoxicity

To explore the synergistic therapeutic effect of AIPH-Ink-GA-ALG hydrogel with or without NIR irradiation, CCK-8 kit was used. Firstly, HCT116 cells were seeded in 96-well plates and cultured for 24 h. Afterwards, HCT116 cells treated with different groups and different concentrations for 12 h. The medium was removed and CCK-8 kit was added into each well for another 1 h.

The death of HCT116 cells induced by different dosage forms was qualitatively evaluated by Calcein-AM/PI co-staining. 1.5×10^5 cells were inoculated in a confocal dish with a diameter of 20 mm. The cells were incubated to make them adhere to the wall and were randomly divided into different groups. Then different preparations (AIPH (60 μg/mL), Ink (25 μg/mL), ALG (1 mg/mL), GA (1 μg/mL)) were added into the dishes for 1 h. They were irradiated with or without a 1064 nm laser for 10 min and cultured for another 12 h. The cells were stained with a Calcein-AM/PI probe (4 mmol/L at 37 °C for 15 min) and observed with a confocal microscope. ImageJ software was used for fluorescence semi-quantification to compare the proportion of living and dead cells.

2.7. Lipidomic analysis

First, HCT116 cells were plated in a culture dish (10^5 cells/well) and incubated with DMEM for 24 h. HCT116 cells were subjected to different treatments (control, GA, ALG–Ink, ALG–Ink–AIPH–GA) with or without 1064 nm laser for 10 min and incubated for another 6 h. Cells were collected for the following operations. 1. To the 2 mL EP tube containing each cell, add 750 μL chloroform methanol (2:1) solution (- 20 °C), add 100 mg glass beads, vortex oscillation for 30 s, put the centrifuge tube containing the sample in the 2 mL adapter of the instrument, immerse it in liquid nitrogen for 5 min, take out the centrifuge tube, freeze and thaw it at room temperature on the double-sided plate, put the centrifuge tube in the 2 mL adapter again, install it in the grinder, and oscillate for 2 min at 50 Hz; 2. Place on the ice for 40 min, add 190 μL H2O, vortex for 30 s, 3. Centrifuged at 12000 rpm for 5 min and take 300 μL of the precipitate, 4. Add 500 μL of Chloroform methanol mixed solution (pre-cooled at -20 °C), 5. Centrifuged at 12000 rpm for 5 min and take 400 μL of the precipitate. The sample was concentratedly dried in a vacuum drying oven, 6. Dissolve samples with 200 μL isopropanol, and the supernatant was filtered through 0.22 μm membrane to obtain the prepared samples for LC-MS.

2.8. Immobilization of in-situ hydrogels

To assess the immobility of the hydrogels in vivo, nude mice were injected subcutaneously with 60 μl of ICG or ALG–ICG (ICG 200 μg/mL, ALG 5 mg/mL). The drug diffusion was observed with a fluorescence imaging system. Meanwhile, two groups of nude mice were injected with 60 μl of Ink and ALG–Ink (Ink 200 μg/mL, ALG 5 mg/mL) subcutaneously to observe the diffusion of the drug in the body. After 48 h, photos of the incision of the skin tissue were taken.

2.9. Photothermal effect in vivo

Different groups (PBS, Ink–ALG, AIPH–Ink–ALG, GA–ALG, ALG–Ink–GA, Ink–AIPH–GA, ALG–Ink–AIPH–GA) were irradiated with a 1064 nm laser for 10 min ($0.5 W/cm^2$), and the thermal imaging system was exploited to record temperature.

2.10. Detection of GSH

Firstly, HCT116 cells were plated in the 6-well plate (2×10^5) and cultured for 24 h. The different groups were treated with equal concentration for 1 h. Then, they were irradiated with a 1064 nm laser ($0.5 W/cm^2$) for 10 min and incubated for another 11 h. Secondly, the cells were washed with pre-cold PBS and collected with a cell scraper. Subsequently, the cells were lysed for 20 min with Triton-X-100 lysis buffer and centrifuged for 10 min (1000G 4 °C). As a final point, the supernatant (50 μL) was mixed with 200 μL DTNB (200 μM) for 30 min, and the absorbance was measured by microplate analyzer at 412 nm. GSH was evaluated in vivo with the same method.

2.11. Western blot

Briefly, HCT116 cells were inoculated on 6-well plates (1.5×10^5) for 24 h. Then, different groups at an equivalent concentration ((AIPH (60 μg/mL), Ink (25 μg/mL), ALG (1 mg/mL), GA (1 μg/mL)) were treated with HCT116 cells. After incubation for 8 h, the cells were washed three times with PBS, collected, and lysed. The lysates of the cells were operated in accordance with the standard instructions. GAPDH was used as a control.

2.12. In vivo antitumor study

The mice were randomly divided into 6 groups (PBS, Ink–ALG–laser, AIPH–Ink–ALG–laser, GA–ALG–Laser, GA–Ink–ALG–Laser, GA–Ink–AIPH–ALG–Laser, GA–Ink–AIPH–ALG–Fer-1–Laser) when the tumor volume reached 100 mm^3 (n = 5). The drug was injected intratumorally on day 0 and irradiated with a1064 nm laser. After laser irradiation (day 0), tumor volume and body weight of mice were recorded every other day for 15 days. The second irradiation was performed with a 24 h interval from the first irradiation. After 15 days, the tumor and main organs were taken out for hematoxylin and eosin (H&E) and TUNEL staining to evaluate the anti-tumor effect and biological safety. Tumor growth inhibitory rate (IR) and tumor volume were separately calculated with the below formulas.

$$V\left(mm^3\right) = 0.5 \times W^2 \times L$$

$$IR = \left(W_{blank} - W_{treat}\right) / W_{blank} \times 100\%$$

2.13. Statistical analysis

Statistical differences between the two groups were assessed with the unpaired student t-test. Multiple group comparisons were performed by the Bonferroni test for two-way ANOVA. *P < 0.05, * *P < 0.01, * * *P < 0.001 was considered statistically significant and ns represented no significance. All data are expressed as mean ± standard deviation.

3. Results and discussion

3.1. Characterization of the GA-AIPH-Ink-ALG hydrogel

ALG is a water-soluble polysaccharide that can be cross-linked with the physiological concentration of Ca^{2+} to rapidly form hydrogels [66]. To explore the influence of ALG concentration on the formation of hydrogels, various concentrations of ALG solution with a constant concentration of Ink were administered to the simulated physiological concentration of Ca^{2+} solution (1.8 mM) [52]. The Ink was used not only as a photothermal reagent, but also as a visual indicator for observing whether gelatin was formed. As shown in Fig. S1, gel formation depended on the increase of ALG concentration. When the concentration of ALG was only 1 mg/mL, the mixture diffused rapidly at the bottom of the cup due to its weak gelation. With the increase of ALG concentration to 5, 10 and 20 mg/mL, the ALG–Ink mixture quickly turned into the gel in the Ca^{2+} solution. Within half an hour, the shape of the hydrogel barely altered. By comparison, free Ink was injected into an aqueous solution containing Ca^{2+}, and Ink rapidly dispersed throughout the solution (Fig. 1A). Two hours later, the ALG–Ink gel could be easily picked up. It is worth noting that when the concentration of ALG was >5 mg/mL, the viscosity was too large and not conducive to injection. However,

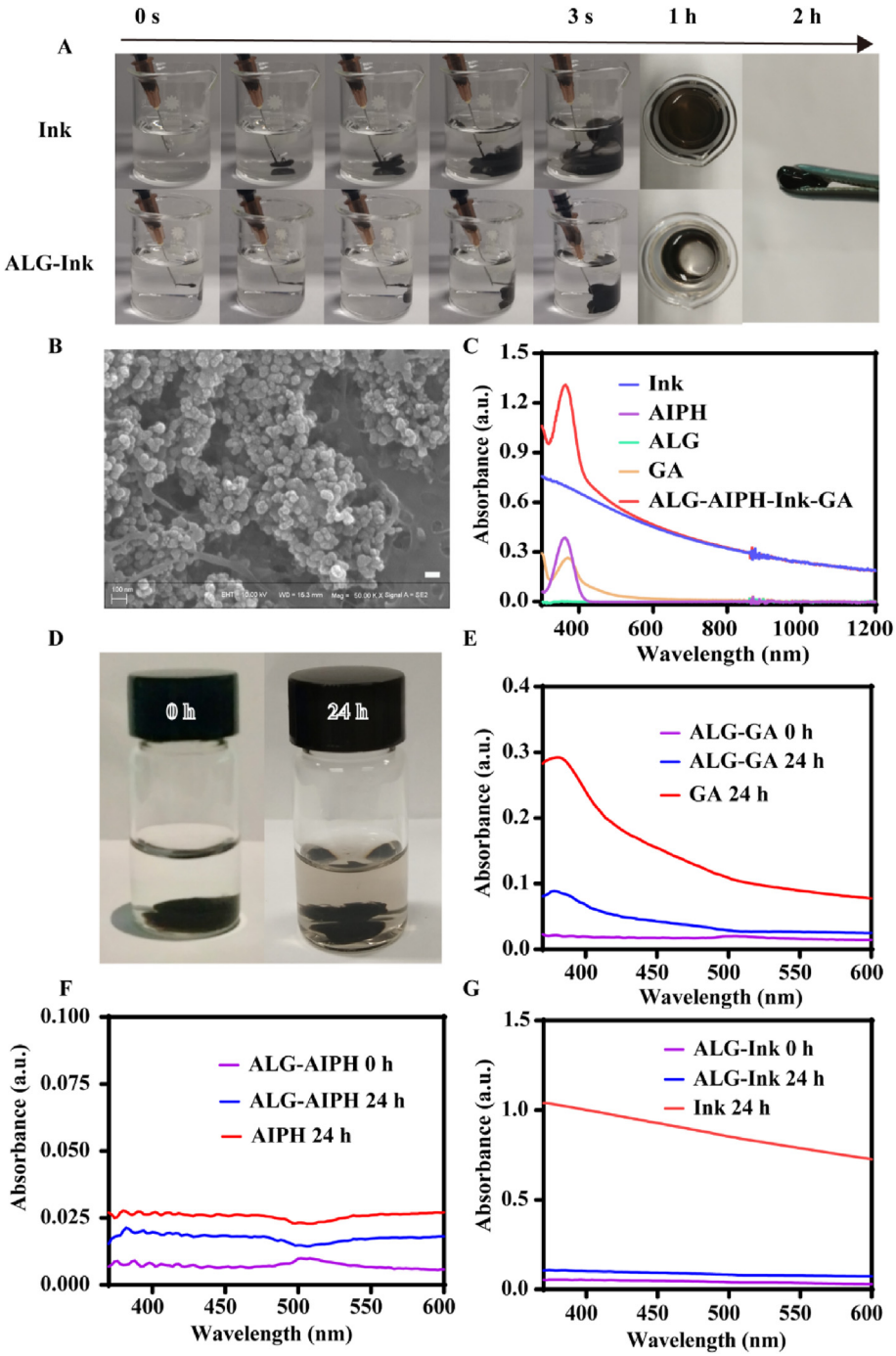

Fig. 1. Characterization of GA–AIPH–Ink–ALG hydrogel. (A) Photographs of Ink and ALG-Ink fluid after being injected into the Ca^{2+}-containing solution at different times (ALG 5 mg/mL). (B) SEM image of GA–AIPH–Ink–ALG, scale bar = 100 nm. (C) The UV–Vis–NIR spectra of different solutions. (D) The appearance of drug release changed at 0 h and 24 h. UV–Vis measured the release of GA (E), AIPH (F), and Ink (G) from ALG after 24-h of shock.

5 mg/mL of ALG was added to the Ca^{2+} solution to form a hydrogel with weaker mechanical intensity and variable morphology. Based on the above results, ALG concentration of 5 mg/mL was selected for subsequent experiments.

The results of dynamic light scattering indicated that the hydrodynamic diameter of the aqueous dispersion of the Ink was approximately 176.3 nm and the zeta potential was approximately −14.033 mV (Fig. S2). This result was similar to that in a previous report [60]. Next, SEM was employed to characterize the morphology of hydrogels. As shown in Fig. 1B, a large number of Ink nanoparticles gathered on the surface of the gel, indicating that the cross-linking between ALG and Ca^{2+} could effectively fix Ink nanoparticles. We used UV–Vis to measure the absorbance of AIPH, Ink, ALG, GA, and AIPH–Ink–GA–ALG. As shown in Fig. 1C, Ink had a higher absorbance from 300 nm to 1200 nm, which proved that Ink could be used as a photothermal agent. ALG had almost no absorbance, AIPH and GA had strong absorption peaks at 360 nm and 370 nm, respectively, but the mixed solution had the absorption characteristics of AIPH, GA, and Ink, which verified that AIPH, GA, and Ink were encapsulated in ALG cross-linked with Ga^{2+}. Constant temperature oscillation was employed to mimic the dynamics in vivo, as shown in Fig. 1D, only a small amount of Ink was freed from the hydrogel after 24 h. To further investigate the release of the drug from hydrogel, a UV

spectrophotometer was applied to investigate the absorption spectra of GA, Ink, and AIPH in the supernatant of the released solution. At 0 h, UV–Vis absorption hardly appeared owing to no drug discharge. After 24 h, the distinctive absorbance of GA, Ink, and AIPH emerged (Fig. 1E–G), showing that small amounts of GA, Ink, and AIPH were liberated from the ALG. However, the absorbance was much lower than free-GA, Ink, and AIPH. The results demonstrated that the gel was an untight structure, which was similar to the literature report [52].

3.2. Photothermal effects and extracellular free-radical detection

Ink has strong absorbance in the second near-infrared (NIR-II), which inspired us to explore the photothermal properties of different groups [60]. As presented in Fig. 2A, with the concentration of Ink increasing, the temperature of the solution also increased in a dose-dependent manner, indicating that the photothermal performance depended on the concentration of the Ink. For instance, the temperature of Ink at a concentration of 25 μg/mL increased from 26.90 °C to 44.80 °C after 10 min of 1064 nm laser irradiation. To achieve low-temperature PTT,

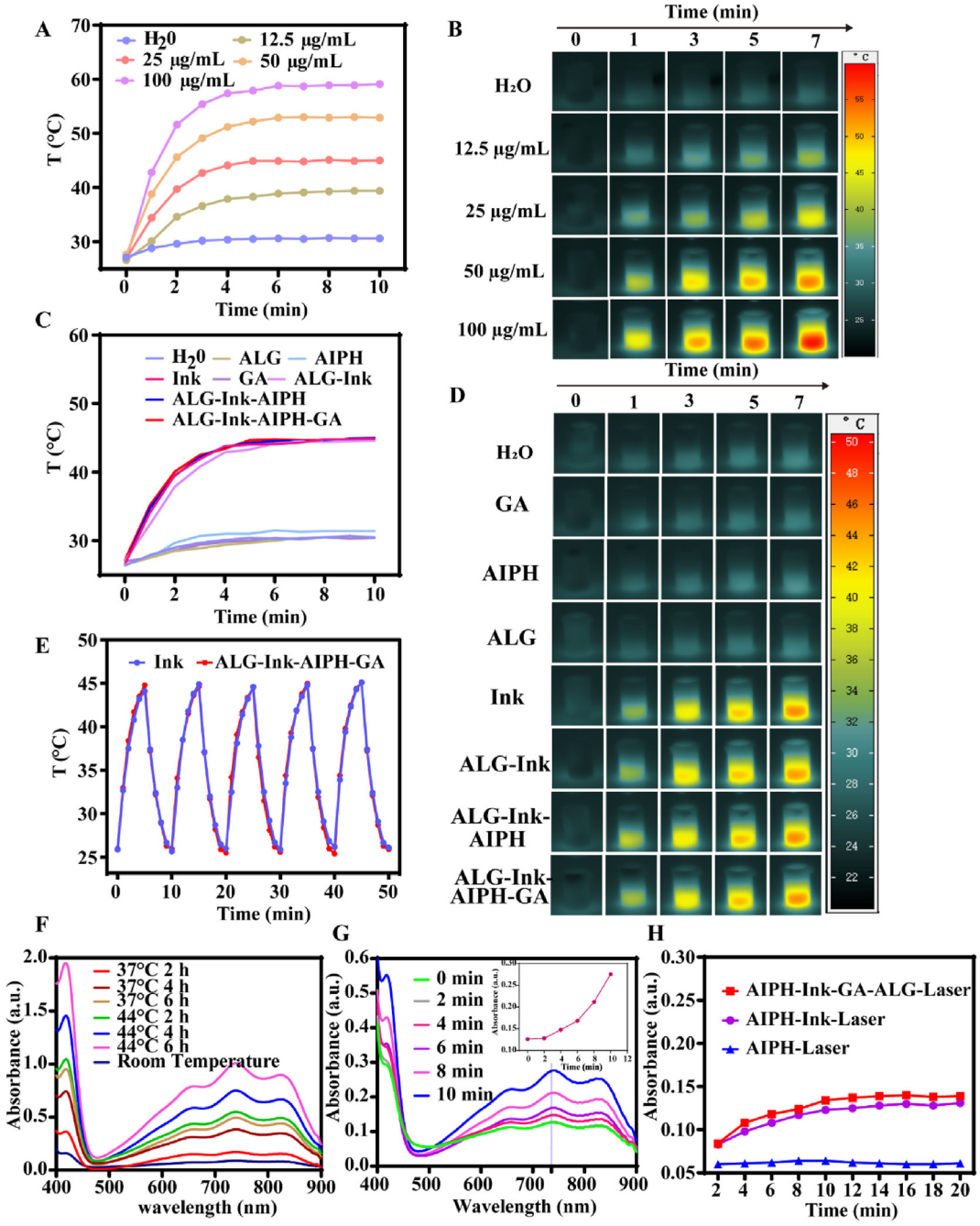

Fig. 2. Photothermal conversion property and free radical release. (A) The temperature curves of Ink at various concentrations under 1064 nm laser (0.5 W/cm^2) irradiation (the initial mean temperature was 26.98 °C) and (B) corresponding photothermal images. (C) The temperature change of different groups with 1064 nm laser (0.5 W/cm^2) irradiation (the initial mean temperature was 26.74 °C) and (D) representative photothermal images. (E) Cycle stability of GA–AIPH–Ink–ALG and Ink. (F) The generation of $ABTS^{+\bullet}$ in ABTS and AIPH at different temperatures and times. (G) The absorption of $ABTS^{+\bullet}$ produced from the reaction of ABTS and GA–AIPH–Ink–ALG under 1064 nm (0.5 W/cm^2) laser irradiation for different times. (F) The absorbance of different groups at 736 nm with a prolonged 1064 nm laser irradiation time.

we ultimately selected the concentration of Ink as 25 μg/mL for subsequent research. The temperature changes were detected by infrared thermal imaging device (Fig. 2B). The photothermal effect of Ink and its hydrogel mixed solution were also explored (Fig. 2C and D). For a constant concentration of Ink (25 μg/mL), the temperature of Ink, ALG–Ink, ALG–Ink–AIPH and ALG–GA–AIPH–Ink groups increased notably, and the temperature rise was substantially the same, attaining approximately 44 °C, whereas a negligible temperature rise was detected for the separate GA, H_2O, AIPH, and ALG components under the same laser irradiation conditions. Furthermore, photothermal stability was also evaluated by recording the temperature curve of the Ink and GA–AIPH–Ink–ALG solution. As displayed in Fig. 2E, no obvious damping was observed during the unabridged procedure, emphasizing the superior photothermal stability of Ink and GA–AIPH–Ink–ALG solution. In addition, it showed that GA, AIPH, and ALG did not affect photothermal stability. The above results confirmed that Ink could be used as an effective photothermal agent for NIR–II–triggered AIPH decomposition.

The decomposition capability of AIPH was explored by measuring the UV–Vis spectrum of $ABTS^{+\bullet}$. As a probe, ABTS could react with alkyl radicals to produce green $ABTS^{+\bullet}$, which has a typical UV absorption peak in the range of 400–900 nm. The relationship between the formation of $ABTS^{+\bullet}$ and temperature was explored when ABTS and AIPH were incubated for the identical time. As presented in Fig. 2F, when ABTS and AIPH react at the same temperatures, the generation of $ABTS^{+\bullet}$ was closely related to time. However, under equal incubation times, the concentration of $ABTS^{+\bullet}$ at 44 °C was notably higher than that at 37 °C, demonstrating that the disintegration rate of AIPH was quicker at elevated temperatures. Furthermore, the $ABTS^{+\bullet}$ production capability was investigated by incubating ABTS with GA–AIPH–Ink–ALG under 1064 nm laser irradiation for different times (Fig. 2G). The absorbance of $ABTS^{+\bullet}$ increased with prolongation of the laser irradiation time. $ABTS^{+\bullet}$ had a characteristic absorption peak at 736 nm. The absorption peak of $ABTS^{+\bullet}$ at 736 nm was time dependent, which demonstrated that the release of R• increased with prolonged irradiation time (Fig. 2G). A microplate reader was used to measure the absorbance at 736 nm of AIPH–Ink and GA–AIPH–Ink–ALG irradiated at different times. As shown in Fig. 2H. When the irradiation time was <10 min, the absorbance of AIPH–Ink and AIPH–Ink–GA–ALG increased with the prolongation of the irradiation time, whereas when the irradiation time was >10 min, the absorbance slightly changed, indicating that the release of AIPH peaked when irradiated for 10 min. Moreover, the absorbance of the AIPH group showed almost no increase, indicating that the decomposition of AIPH was due to the photothermal conversion of Ink upon 1064 nm laser irradiation.

3.3. In vitro antitumor effect

To explore the antitumor effect in vitro, CCK-8 assays were utilized to investigate cell vitality. Firstly, HCT116 cells were incubated with dissimilar concentrations of AIPH, Ink, or ALG. As shown in Fig. S3A, there was almost no obvious cytotoxicity to HCT116 cells after 24 h even though the concentrations of AIPH, Ink, and ALG reached 200 μg/mL, 400 μg/mL, and 2 mg/mL correspondingly, indicating that AIPH, Ink, and ALG have excellent biocompatibility. While when GA was incubated with HCT116 cells, the cell viability uninterruptedly declined with increasing GA concentration, showing that GA had obvious cytotoxicity. Furthermore, we evaluated the cytotoxicity of different groups to HCT116 cells in the presence or absence of 1064 nm laser irradiation. As Fig. S3B shows, free AIPH did not cause significant cytotoxicity. In the Ink group, when the concentration reached 25 μg/mL, the cell survival rate was 71.60% after 10 min of the 1064 nm laser irradiation (Fig. S3C), showing that low-temperature PTT alone had only a feeble antitumor effect. Successively, the synergistic therapeutic effect of AIPH–Ink with or without 1064 nm laser irradiation was assessed. As displayed in Fig. 3A, the cell viability continued to decrease with the increasing concentration of AIPH under laser irradiation. When the concentration of AIPH increased to 200 μg/mL, cell viability decreased to 25.60%, and no evident cytotoxicity was observed without laser, indicating that cell cytotoxicity was caused by the thermal disintegration of AIPH into alkyl radicals. This result was consistent with our previous research results. AIPH was decomposed into cytotoxic R• by laser irradiation in the presence of the photothermal agent and induced apoptosis through lipid oxidation [33]. Another study used AIPH-loaded mesoporous silica on the surface of two-dimensional Nb2C MXene nanosheets to induce tumor cell apoptosis through thermally decomposed AIPH in the hypoxic tumor microenvironment [32]. Next, to corroborate the synergy effect between GA and Ink, GA with or without laser was examined. As shown in Fig. 3B and C, there was no obvious difference between the GA–Laser and GA groups. Nevertheless, the cell viability of the GA–Ink–Laser group (Ink concentration of 25 μg/mL) decreased continuously with increasing GA concentration. When the concentration of GA reached 2 μg/mL, the corresponding cell viability decreased to 14.9%. In addition, the half maximal inhibitory concentration (IC_{50}) of GA–Ink–Laser (0.83 μg/mL) in HCT116 cells was lower than that of the GA–Laser (0.93 μg/mL) group. The above results implied that the synergistic effect of GA and Ink augmented the antitumor effect. Previous studies have shown that GA and HSP90 had specific binding sites that could inhibit the expression of HSP90 [61,62]. Therefore, we speculated that the synergy effect was related to the expression of HSP90. The western blot experiment showed the expression of HSP90 in cells. As illustrated in Fig. 3I, S4, the expression of HSP90 in the Ink–Laser and AIPH–Ink–Laser groups improved notably compared with the control group, indicating that laser-induced low-temperature photothermal increased the expression of HSP90. However, the level of HSP90 in the GA–Ink–Laser group decreased significantly, indicating that GA could inhibit HSP90. Moreover, compared with the AIPH–Ink–Laser group, the GA–AIPH–Ink–Laser and GA–AIPH–Ink–ALG–Laser groups revealed decreased levels of HSP90, which further verified that GA could bind HSP90. Finally, the synergistic antitumor effects of AIPH, Ink, and GA were also investigated. As illustrated in (Fig. 3D and E), the GA–AIPH–Ink–ALG and GA–AIPH–Ink group with laser irradiation both exhibited predominant cytotoxicity under the same conditions. Notably, for free GA with laser irradiation, when the concentration was up to 1 μg/mL, the cell viability reached 50.10%. For the GA–AIPH–Ink–ALG and GA–AIPH–Ink groups with laser irradiation, the cell viability was lower compared to GA–Laser group. Furthermore, in the IC_{50} graph (Fig. 3F), the cytotoxicity increased with lower concentrations of the GA–AIPH–Ink–ALG–laser (0.39 μg/mL) and GA–AIPH–Ink–laser (0.49 μg/mL) groups relative to those of the GA–Laser group (0.93 μg/mL). As expected, the synergistic therapeutic effects of free radicals and GA was most effective at triggering tumor cell death. To further corroborate the ability to inhibit tumor cells, live and dead staining assays were performed to intuitively observe the living and dead cells by confocal fluorescence imaging. As presented in Fig. 3G and H, no obvious red fluorescence could be detected for the cells treated with 1064 nm laser alone or in the AIPH–Laser and AIPH–Ink groups, suggesting that the Laser, AIPH–Laser, and AIPH–Ink groups had enervated ability to kill HCT116 cells. The cells incubated with GA, GA–Ink, AIPH–Ink exposed to a 1064 nm laser, a portion of dead cells was observed, and the proportions of dead cells were 12.80%, 43.23%, and 24.32%, respectively. When the HCT116 cells were treated with GA–AIPH–Ink–ALG or GA–AIPH–Ink with a 1064 nm laser, almost all of the red fluorescence was observed, showing that GA–AIPH–Ink–ALG and GA–AIPH–Ink with 1064 nm laser had excellent antitumor effects, and the cell death rates were 93.38% and 97.64%, respectively. These results indicated that GA combined with AIPH, Ink, and PTT had synergistic antitumor effects in vitro.

3.4. Mechanism of GA–AIPH–Ink–ALG-induced ferroptosis in vivo

To investigate the synergistic antitumor mechanism of GA–AIPH–Ink–ALG, we analyzed how GA–AIPH–Ink–ALG induces cell death. Previous studies have shown that GSH was highly expressed in tumors to

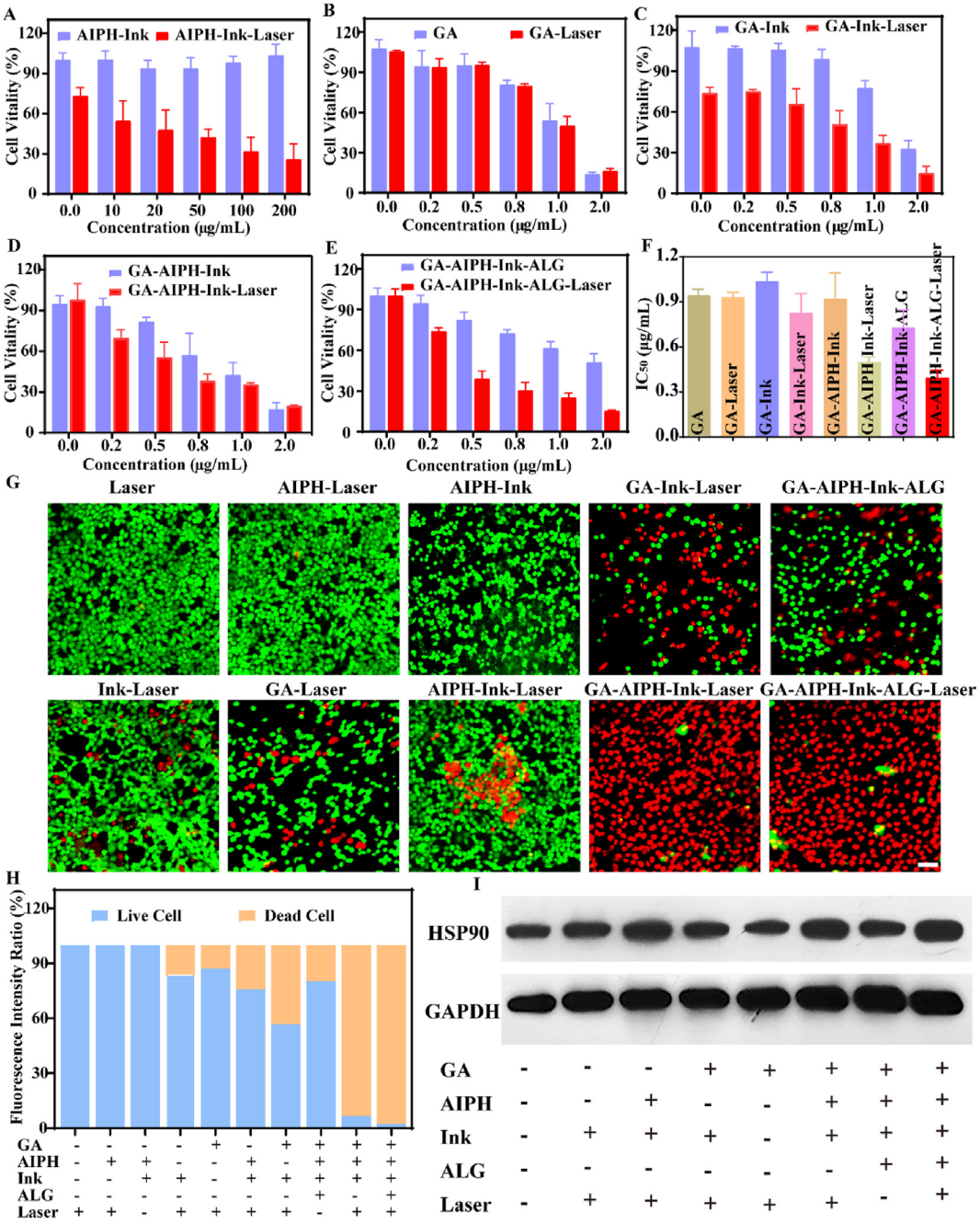

Fig. 3. Synergistic treatment of GA–AIPH–Ink–ALG in vitro. (A) Corresponding cell viability after being treated with an increasing concentration of AIPH and constant concentration of Ink. (B) Cell activity after dealing with elevated concentration of GA. (C) Cell viability after treatment with different concentrations of GA and stable concentration of Ink. (D) Cell viability after treatment with different concentrations of GA and constant concentration of Ink and AIPH. (E) Cell viability after treatment with different concentrations of GA and Changeless concentration of Ink, AIPH, and ALG (all of the above groups were divided into with and without 1064-nm laser (0.5 W/cm^2) irradiation groups) (F) IC_{50} of different groups. (G) Confocal images of HCT116 cells co-stained Calcein -AM (green) and PI (red) after incubation with different groups (scale bars = 50 μm) and (H) corresponding semi-quantitative analysis of (G). (I) Western blot expression of HSP90 after incubation with HCT116 cells in different groups.

achieve rapid tumor proliferation and redox balance. Therefore, the consumption of GSH could break the redox balance and achieve a better therapeutic effect [7,67]. In addition, rapid consumption of GSH could inhibit the GPX4 expression, which was a cofactor, and inhibited the conversion of toxic LPO to nontoxic hydroxyl compounds (LOH), thus resulting in ferroptosis [5]. We hypothesized that GA–AIPH–Ink–ALG hydrogels induce cell death by way of ferroptosis. To verify our conjecture, HCT116 cells were treated with Ferrostatin-1 (Fer-1) (Ferrostatin 1 inhibits iron-dependent cancer cell death by blocking cystine transport and glutathione production) and deferoxamine mesylate (DFO) (DFO is an iron sequestrant that captures free iron and prevents it from participating in chemical reactions) (Fig. 4A S5), and it was found that Fer-1 significantly reversed GA–AIPH–Ink–ALG-induced cell death in a concentration-dependent manner. When the concentration of Fer-1 reached 20 μM, the cell viability reached 75.86%, showing that GA–AIPH–Ink–ALG-induced cell death was associated with ferroptosis. However, DFO did not achieve the same effect, suggesting that GA–AIPH–Ink–ALG induced cell death through the System–XC pathway [68,69] rather than through the Fenton response ($Fe^{2+} + H_2O_2 \rightarrow Fe^{3+} + OH^- + \cdot HO$) [70,71]. Subsequently, the intracellular GSH level was

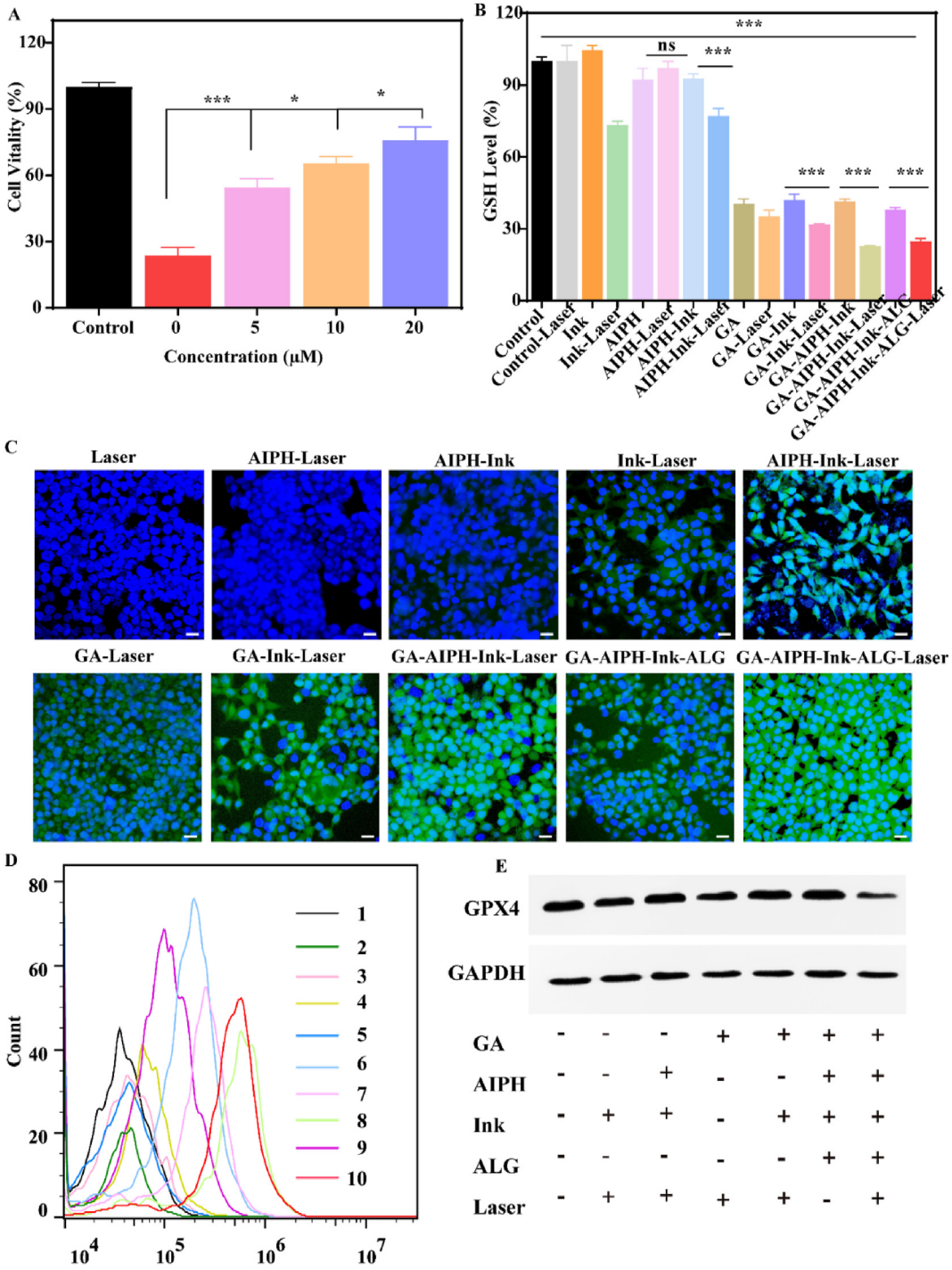

Fig. 4. Analysis of ferroptosis in vitro (A) Cell viability of HCT116 cells after being treated with an elevated concentration of Fer-1 and constant concentrations of GA, AIPH, Ink, and ALG under 1064 nm laser irradiation. (B) Quantitation of GSH levels in HCT116 cells with different treatments (n = 4). (C) ROS generation of HCT116 cells with various treatments detected by CLSM. (D) Flow cytometer analysis of ROS generation under different conditions (DCFH-DA as the detection probe) (1: control 2: Ink–Laser 3: AIPH–Laser 4: GA–Laser 5: AIPH–Ink 6: AIPH–Ink–Laser 7: GA–Ink–Laser 8: GA–AIPH–Ink–Laser 9: GA–AIPH–Ink–ALG 10: GA–AIPH–Ink–ALG–Laser). (E)The expression of GPX4 in HCT116 cells treated with different formulations.

further detected after diverse treatments by DTNB (Fig. 4B). As expected, compared with the control group, the expression of GSH did not decrease significantly in AIPH with or without laser irradiation. Contrasted with the Ink and AIPH–Ink groups, the Ink–Laser and AIPH–Ink–Laser groups showed a slight decrease, whereas the relative intracellular GSH level of the GA groups obviously decreased and the GA–AIPH–Ink–laser group had the best GSH depletion ability. These results demonstrated that GA combined with AIPH weakened the antioxidant capacity of cells, leading to enhanced ROS to achieve synergistic antitumor therapy.

The redox capacity and oxidation level in the cell always maintain a dynamic balance. The decrease in the oxidation reduction level will upset this balance and may result in an increase in the oxidation level [48]. The intracellular ROS level was detected by DCFH–DA, which can be oxidized by free radicals to produce strong green fluorescence. As displayed in

Fig. 4C, no obvious green fluorescence was observed in the Laser, AIPH–Laser, and AIPH–Ink groups, whereas the AIPH–Ink and GA–Ink groups with 1064 nm laser irradiation had a weak green-fluorescence signal, exposing that the two groups could produce trace amounts of ROS. Interestingly, after treatment with GA–AIPH–Ink–ALG or GA–AIPH–Ink under 1064 nm laser irradiation, the cells exhibited brighter green fluorescence due to the consumed GSH and decomposed AIPH. Moreover, this result also showed that ALG had good biocompatibility and did not affect the production of ROS. To further quantitatively analyze free radicals, HCT116 cells were treated with different formulations and the cells were stained with DCFH-DA and analyzed by flow cytometry. As displayed in Fig. 4D, when conjoined GA with AIPH, nearly ten times stronger fluorescence intensity compared to the control group was discovered, demonstrating the generation of large number of ROS. It's worth noting that according to the flow cytometer results. Compared with the AIPH–Ink–Laser group, the GA–Ink–Laser group revealed a slightly better fluorescence intensity, which may be attributed to the consumption intracellular GSH by GA [46]. The consumption of GSH, on the one hand, was beneficial to the generation of ROS in cells. On the other hand, it could inactivate GPX4, both of which weaken the antioxidant barrier. GPX4 was a coenzyme that could degrade toxic LPO to nontoxic LOH in the presence of GSH. Thus, as the key protein of ferroptosis, GPX4 played a crucial role in the process of ferroptosis. After the cells were treated with different formulations, the expression of GPX4 in the cells was explored by western blot. As exhibited in Fig. 4E, S6 GA–AIPH–Ink–Laser and GA –AIPH–Ink–ALG–Laser treatment significantly reduced the expression of GPX4, indicating that the synergy of GA and AIPH was achieved through GPX4. Consequently, our results confirmed that GA–AIPH–Ink–ALG could be realized to boost ferroptosis by consuming GSH and accumulating ROS.

3.5. Lipidomic analysis

As is well known, free radicals tend to react with biomolecules containing lipid, protein, and inherited information ingredients [72]. As a vital part of cytomembranes, lipids play a significant part in maintaining cell activity, providing energy, and participating in information exchange [73]. The key to ferroptosis is the accumulation of LPOs in the cell membrane [74]. Thus, liquid chromatography–mass spectrometry (LC-MS) was used to detect changes in the lipid composition of cells after treatment with different formulations. After data preprocessing, the lipids obtained by annotation were classified into 10 categories according to lipid chains and groups (Fig. 5A). Principal Component Analysis (PCA) (Fig. 5B) was applied to detect the degree of aggregation and dispersion of observable samples, which showed that the control group and GA–Laser group were mainly concentrated in the positive direction, whereas the GA–Ink–Laser and GA–AIPH–Ink–Laser groups were primarily gathered in the opposite direction. Orthogonal projections to latent structures discriminant analysis were performed, and the results also showed that different groups gathered in different quadrants, which was consistent with the PCA result (Fig. S7). Thereafter, the agglomerated hierarchical cluster analysis processed the cells after treatment in different groups, and the thermogram showed upregulation and downregulation of related lipid expression (Fig. 5C). Furthermore, the number of different metabolites in different groups and the upregulation (red) or downregulation (blue) of metabolite expression was exhibited in Fig. 5D. A Venn diagram visually shows the similarity and overlap of different metabolite compositions in different comparison groups (Fig. S8). Studies have shown that polyunsaturated fatty acids (PUFAs) are the chief targets of many free radicals [5,26,75,76]. Therefore, the changes of cellular PUFAs after treatment with different formulas were compared.

Phosphatidylethanolamines (PEs) and phosphatidylcholines (PCs) are more susceptible to oxidation. The results showed that several oxidized PEs and PCs, such as PE (14:1e_21:0), PE (16:1e–21:0), PE (35:1e), PE (37:4e), PE (37:5e), PE (39:5e), PC (16:1_14:1), PC (16:1_16:1), PC (16:2e_18:0), PC (16:2e_20; 3), PC (18:0_18:1) and PC (32:4) correspondingly increased (Fig. 5F–G, Fig. S9A–B). In addition, after GA–AIPH–Ink–Laser treatment of HCT116 cells, lipid oxidation levels in some types of PS and LPC also increased, indicating that lipid oxidation occurred in the cell membrane (Fig. S9C and S10A–B). Finally, differential lipid association analysis was used to study the consistency of changing trends between lipids (Fig. 5D). The results showed that the change trend of certain lipids was the same, showing a positive correlation.

3.6. Fixation ability of hydrogel in vivo

As is well known, intratumor injection of drugs would gradually spread to the interstitial space, causing inescapable secondary action toward the normal tissue neighboring the tumor. In this work, ALG could quickly bind with Ca^{2+} in vivo to form an in-situ hydrogel, which could fix the drug inside the tumor and achieve slow release. To explore the immutability of the in-situ hydrogels, indocyanine green (ICG) was used to observe whether or not the drug had spread into the tissue. Nude mice were subcutaneously injected with 60 μl of ICG and ALG–ICG (ICG 200 μg/mL, ALG 5 mg/mL). In vivo imaging was then performed at diverse time points to detect drug dispersion. As shown in Fig. S11A, free ICG spread to the surrounding tissues at 1 h, whereas the ALG–ICG group could be fixed for 48 h, which proved that hydrogel had an outstanding fixation effect. Consequently, ALG could be used as a carrier for slow release, which potentially could improve drug efficacy. To further demonstrate the feasibility of hydrogel-impregnated drugs, individual Ink or ALG–Ink was injected (Ink 200 μg/mL, ALG 5 mg/mL) and their diffusion was observed. As displayed in Fig. S11B, there was no obvious diffusion of Ink and ALG–Ink at 0 h. At 48 h, Ink had obviously diffused into the surrounding area due to the lack of hydrogel fixation. The subcutaneous incision was performed to observe the drug diffusion. It was observed that the ALG–Ink group stayed at the injection site, whereas only a small amount of the Ink group stayed at the injection site. These results indicated that the ALG hydrogel had a good fixation effect and prevented rapid drug seepage into surrounding tissues.

3.7. Photothermal effects and antitumor effect in vivo

To explore the photothermal performance of the hydrogel in vivo, a near-infrared thermal imager was used to record the temperature. As depicted in Fig. 6A and B, the phosphate-buffered saline (PBS), the GA–AIPH–ALG and GA–ALG groups had only a slight temperature increase owing to the lack of photothermal agent. Compared with the PBS group, the GA–ALG and GA–AIPH–ALG groups had a better temperature-raising effect, which may be due to the thermal insulation effect of ALG after cross-linking with Ca^{2+} in vivo to form the hydrogel. In the GA–AIPH–Ink–ALG–Laser groups, the temperature rose to 44.7 °C after irradiation time for 10 min. The high temperature decomposed the AIPH to R●.

Encouraged by the remarkable in vitro cytotoxicity experimental results, we continued to investigate the antitumor effect in vivo. When the tumors grew to 80–100 cm^3, the nude mice were casually separated into 6 groups. The GA–AIPH–ALG–Laser and GA–AIPH–Ink–ALG groups were not included. Because the GA–AIPH–ALG–Laser and GA–AIPH–Ink–ALG groups lack photothermal agents and laser irradiation, respectively, AIPH could not be degraded. Therefore, GA was show to have the main antitumor effect in these two groups, which was the same as that in the GA–ALG–Laser group. On day 0, the mice were injected intratumorally and irradiated with a 1064 nm laser for 10 min. The second irradiation was performed after an interval of 24 h. Then, the tumor volume and weight of the mice were recorded every other day for 15 days. The tumors were taken out and photographed, weighed after 15 days (Fig. 6E and F). As exhibited in Fig. 6C, the Ink–ALG–Laser group had a slightly better tumor inhibition effect than that of the PBS group and the tumor suppression rate reached 25.97%. This result is attributed to the fact that low-temperature PTT could delay tumor growth but was insufficient to

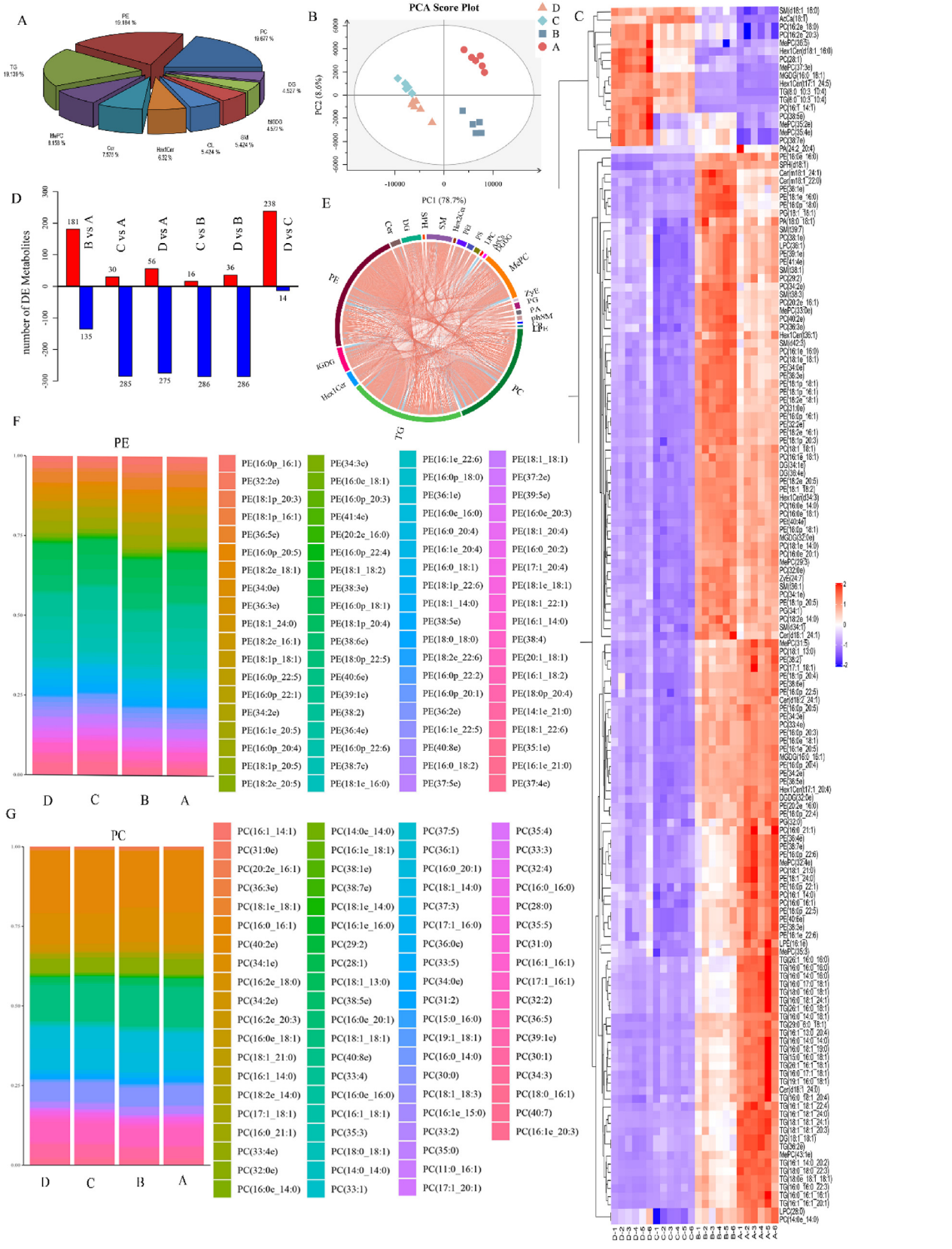

Fig. 5. Lipidomic analysis. (A) Lipid classification of HCT116 cells. (B) PCA analysis of different groups by LC-MS after incubation with various formulations. (C) Hierarchical cluster analysis showing the relative lipid metabolism levels of cells after different treatments. Columns stand for samples and rows stand for lipids. (D) Number of differences in lipid metabolism between different groups. (E) Correlation diagram of different metabolites between different groups. (F–G) Lipids were selected as biomarkers, and the sub-lipid components of two major distinction lipids (PE and PC) were statistically analyzed. (A: control, B: GA–Laser, C: GA–Ink–Laser, D: GA–AIPH–Ink–Laser).

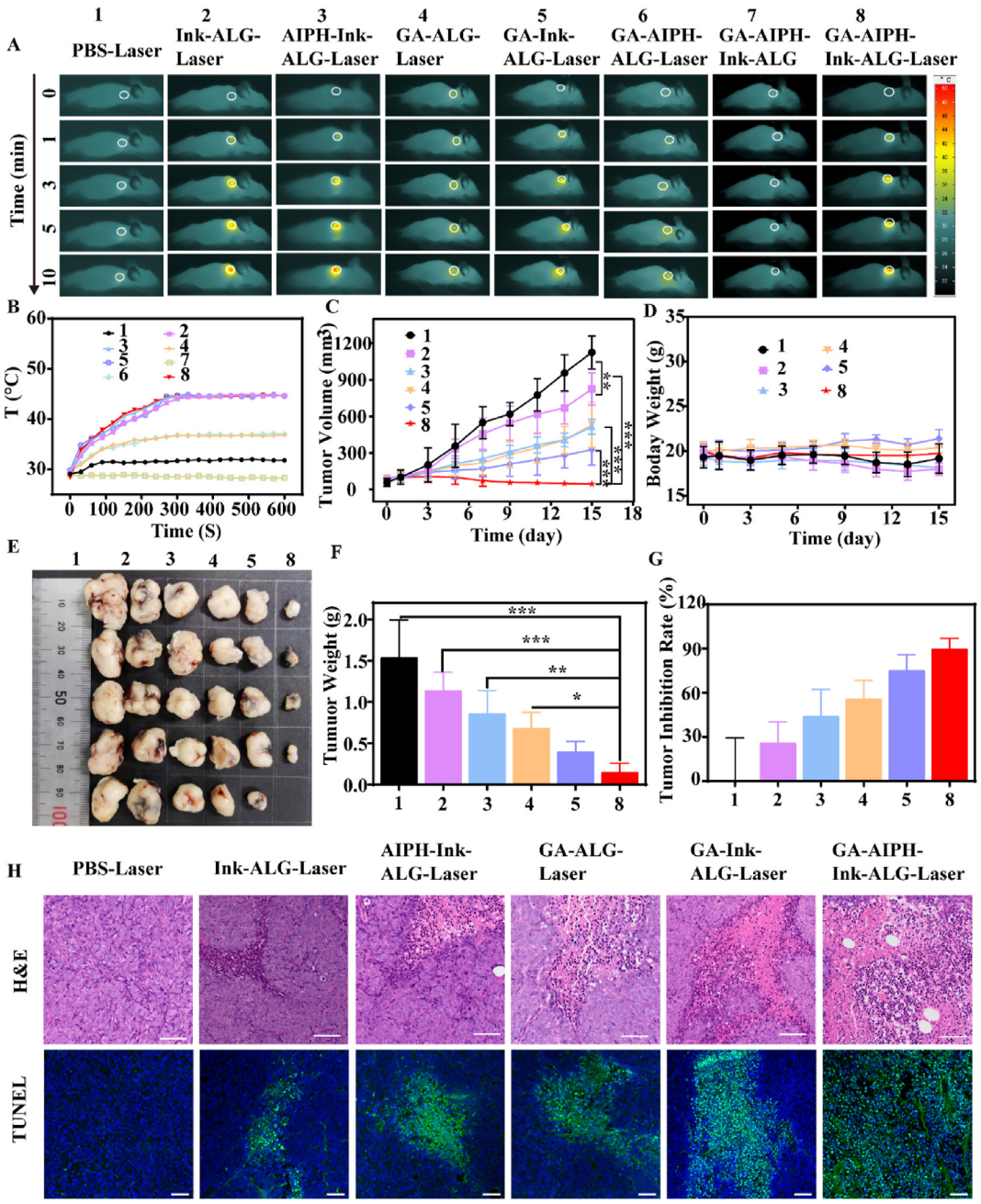

Fig. 6. Photothermal effects and antitumor effect in vivo. (A) Thermal images and (B) temperature curve of the tumor site after 1064 nm laser irradiation for 10 min (0.5 W/cm^2). (C) Tumor-volume changes during treatment period (n = 5). (D) Mean body weight of mice after treatment in different groups during 15 days. The tumor tissue is photographed (E) and weighed (F) after 15 days of different treatments. (G) Inhibition rates of tumor growth with various treatments. (H) Hematoxylin and eosin (H&E) and TUNEL staining of tumor slicing (scale bar of H&E = 50 μm; scale bar of TUNEL = 20 μm).

eliminate tumors [33,59,64]. Moreover, the AIPH–Ink–ALG–Laser and GA–ALG–Laser groups only generated a moderate antitumor effect. Tumor suppression rates reached 44.16% and 55.84%, respectively (Fig. 6G). Notably, with use of GA to deplete tumoral GSH, the GA–AIPH–Ink–ALG–Laser synergistic treatment dramatically inhibited tumor growth and even led to tumor ablation with only two treatments, and the tumor suppression rates reached 90.12%, indicating the superior synergistic effect of GA and AIPH. We further assessed the pathological images of the tumor tissue by H&E and TUNEL staining. As illustrated in Fig. 6H, there were no obvious cells dead in the PBS group and only partial cell death in the Ink–ALG–Laser and GA–Ink–ALG–Laser groups. However, the number of dead cells was the highest in the GA–AIPH–Ink–ALG–laser group, indicating that the GA–AIPH–Ink–ALG hydrogel could efficiently treat HCT116 cells by consuming GSH and increasing ROS in vivo. Moreover, compared with the PBS group, the GA–AIPH–Ink–ALG group showed obvious nuclear pyknosis and the loose-cell arrangement. The body weight of mice in all groups did not show apparent weight loss, reflecting no markedly systemic toxicity during the treatment of the hydrogel (Fig. 6D). Furthermore, histological analysis was also implemented to assess biological safety. As shown in Fig. S12, there were no obvious pathological changes in the heart, liver, spleen, lung, and kidney. Considering all of these results, we concluded that GA–AIPH–Ink–ALG had the most effective potential synergistic antitumor effects in all groups.

3.8. Evaluation GA–AIPH–Ink–ALG in vivo induction of cell death by ferroptosis

To determine if the anticancer effect of GA–AIPH–Ink–ALG in vivo was induced by ferroptosis, Fer-1 was used to co-inject into the tumor. As shown in Fig. 7A, the PBS group showed rapid tumor growth, and the GA–AIPH–Ink–ALG group showed an excellent tumor inhibition effect. However, concurrent injection of the ferroptosis inhibitor Fer-1 group showed rapid recovery of tumor growth ability, showing that Fer-1 inhibited cell death. After therapy, H&E and TUNEL staining were used to evaluate tumor morphology and cell death. As proved in Fig. 7E, the GA–AIPH–Ink–ALG group showed a large area of cell necrosis, proving that GA–AIPH–Ink–ALG could inhibit the propagation of HCT116 cells. Nevertheless, the necrosis of the GA–AIPH–Ink–ALG–Fer-1 group was

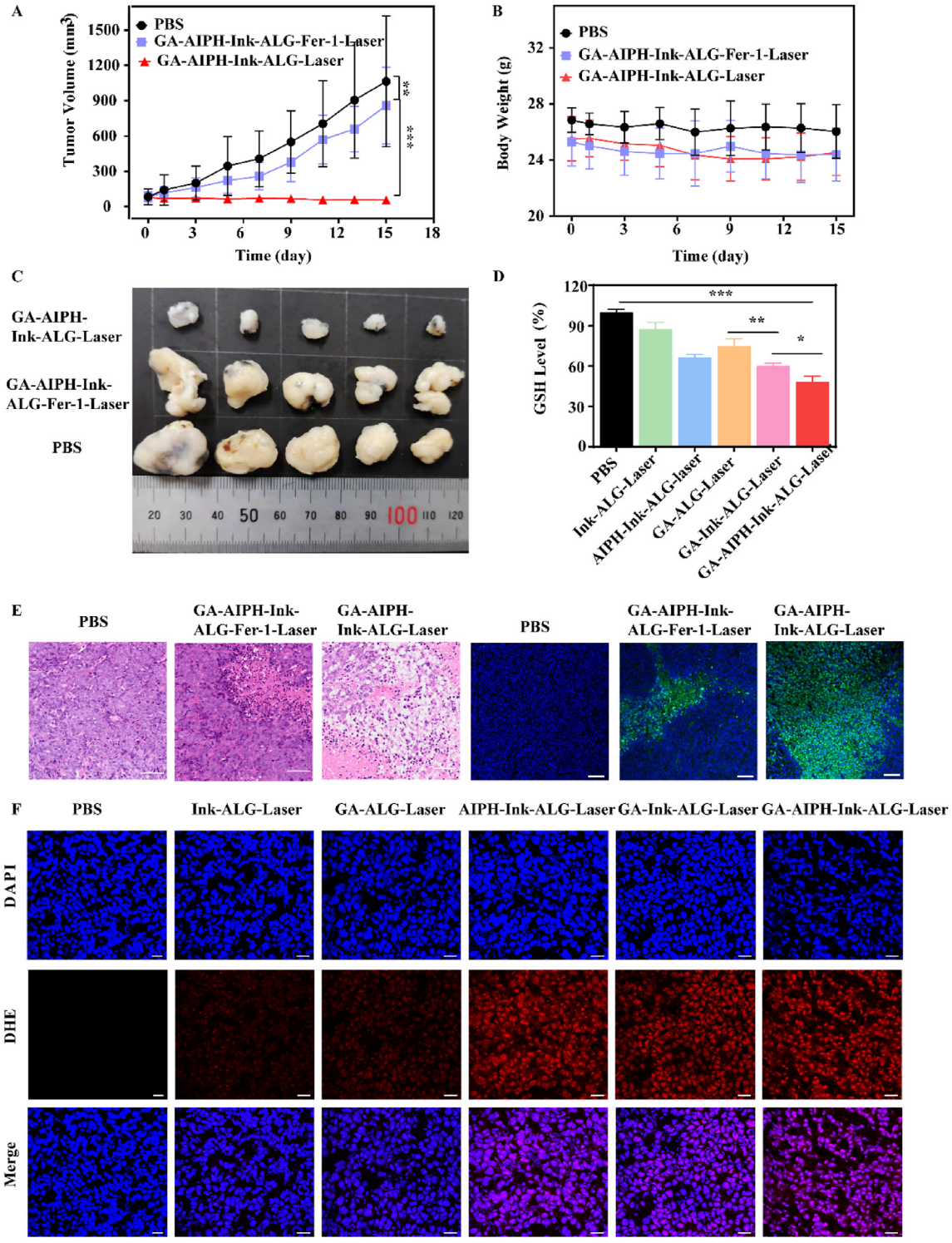

Fig. 7. Mechanical evaluation of GA–AIPH–Ink–ALG–induced ferroptosis in vivo. (A) Tumor volume and (B) body-weight changes during 15 days (n = 5). (C) Tumor tissue were collected and photographed after 15 days of different treatments. (D) GSH levels of HCT116 with different treatments in vivo. (E) H&E and TUNEL staining of tumor sections after various treatments (Scale bar of H&E = 50 μm; scale bar of TUNEL = 20 μm). (F) Relative ROS generation of HCT116 cells after treatment with different groups.

significantly reduced, indicating that cell death was inhibited after co-injection of Fer-1. The TUNNEL experiment showed the same experimental outcomes. After 15 days of therapy, the tumors were removed from the mice, photographed, and weighed (Fig. 7C and Fig. S13). The body weight of mice in all groups did not exhibit a distinct decline, suggesting no obvious systemic toxicity during treatment (Fig. 7B). To further investigate the ability of GA to consume GSH, GSH levels in the tumor were measured. As shown in Fig. 7D, the level of GSH was slightly decreased in the Ink–ALG and GA–ALG with 1064 nm laser groups but significantly decreased in the GA–AIPH–Ink–Laser group compared with that in the PBS group, which was consistent with the in vitro result. The GSH level was lower in the AIPH–Ink–ALG–Laser group than in the GA–ALG–Laser group. This result may be attributable to free-radical-induced cellular oxidative stress, which reduces intracellular antioxidant capacity. When too much oxidative stress leads to abnormal regulation and inability to recuperate, it may also cause disorder and damage [77–79]. This result showed that GA could interrupt the redox balance. To further evaluate the production of ROS in the tumor, DHE staining was performed. As displayed in Fig. 7F, no obvious red fluorescence was detected in the PBS group but slight red fluorescence was observed in the GA–ALG–Laser group, indicating that a small amount of ROS was produced in the GA–ALG–Laser group. In addition, compared with the GA–Ink–laser group and the AIPH–Ink–Laser group, the GA–AIPH–Ink–ALG–Laser group showed the strongest red fluorescence, proving that the GA–AIPH–Ink–ALG–Laser group produced abundant ROS. This result was consistent with the in vitro result. The above experimental results showed that GA–AIPH–Ink–ALG with 1064 nm laser irradiation induced cell ferroptosis to achieve the antitumor effect.

4. Conclusion

In summary, a novel drug delivery system that induces ferroptosis of tumor cells with the use of injectable ALG to encapsulate GA, AIPH, and Ink was proposed. Under low-temperature hyperthermia, AIPH effectively decomposed into alkyl radicals to increase the oxidative stress of cells, and GA consumed GSH and reduced the antioxidant capacity. The simultaneous consumption of GSH and increased ROS upset the redox balance of the cells, which further inhibited the expression of GPX4. Eventually, oxidation of cell membrane lipids occurred, which induced ferroptosis to achieve a synergistic antitumor effect. Furthermore, ALG encapsulated GA and AIPH cross-linked with the Ga^{2+} in the body to form an in-situ hydrogel, which is helpful to the accumulation of the drug at the tumor site but also beneficial to the sustained release of the drug, reducing damage to the surrounding normal tissues. Our data showed that this strategy exhibits superior antitumor effects both in vivo and in vitro. The toxicity assessment proved that this strategy has tremendous biocompatibility and safety. This proof-of-concept synergy treatment strategy provides a strong developmental foundation for the future application of ferroptosis in biomedicine.

Credit author statement

Xiaomin Su: Conceptualization, Investigation, Methodology, Formal analysis, Writing – original draft, Writing – review & editing. Yongbin Cao: Investigation, Methodology, Data curation, Formal analysis, Writing – original draft, Writing – review & editing. Yao Liu: Conceptualization, Investigation, Formal analysis, Writing – original draft. Boshu Ouyang: Investigation, Methodology, Writing – original draft. Bo Ning: Investigation, Methodology, Writing – review & editing. Yang Wang: Formal analysis, Investigation. Huishu Guo: Funding acquisition, Methodology, Project administration, Supervision. Zhiqing Pang: Conceptualization, Funding acquisition, Methodology, Project administration, Supervision. Shun Shen: Conceptualization, Funding acquisition, Methodology, Project administration, Supervision, Writing – review & editing. Journal Preproof.

Declaration of competing interest

The authors declare that they have no known competing financial interests or personal relationships that could have appeared to influence the work reported in this paper.

Acknowledgments

Financial support was provided by Key Projects in Liaoning Province (2020JH2/10300046).

References

[1] J.C. Reed, M. Pellecchia, Ironing out cell death mechanisms, Cell 149 (5) (2012) 963–965, https://doi.org/10.1016/j.cell.2012.05.009.
[2] N. Kong, X. Chen, J. Feng, T. Duan, S. Liu, X. Sun, P. Chen, T. Pan, L. Yan, T. Jin, Y. Xiang, Q. Gao, C. Wen, W. Ma, W. Liu, M. Zhang, Z. Yang, W. Wang, R. Zhang, B. Chen, T. Xie, X. Sui, W. Tao, Baicalin induces ferroptosis in bladder cancer cells by downregulating FTH1, Acta Pharm. Sin. B (2021), https://doi.org/10.1016/j.apsb.2021.03.036.
[3] Y. Liang, L. Zhang, C. Peng, S. Zhang, S. Chen, X. Qian, W. Luo, Q. Dan, Y. Ren, Y. Li, B. Zhao, Tumor microenvironments self-activated nanoscale metal organic frameworks for ferroptosis based cancer chemodynamic/photothermal/chemo therapy, Acta Pharm. Sin. B (2021), https://doi.org/10.1016/j.apsb.2021.01.016.
[4] W. Wang, M. Green, J.E. Choi, M. Gijon, P.D. Kennedy, J.K. Johnson, P. Liao, X. Lang, I. Kryczek, A. Sell, H. Xia, J. Zhou, G. Li, J. Li, W. Li, S. Wei, L. Vatan, H. Zhang, W. Szeliga, W. Gu, R. Liu, T.S. Lawrence, C. Lamb, Y. Tanno, M. Cieslik, E. Stone, G. Georgiou, T.A. Chan, A. Chinnaiyan, W. Zou, CD8(+) T cells regulate tumour ferroptosis during cancer immunotherapy, Nature 569 (7755) (2019) 270–274, https://doi.org/10.1038/s41586-019-1170-y.
[5] X. Jiang, B.R. Stockwell, M. Conrad, Ferroptosis: mechanisms, biology and role in disease, Nat. Rev. Mol. Cell Biol. 22 (4) (2021) 266–282, https://doi.org/10.1038/s41580-020-00324-8.
[6] Y. Liu, W. Zhen, Y. Wang, J. Liu, L. Jin, T. Zhang, S. Zhang, Y. Zhao, S. Song, C. Li, J. Zhu, Y. Yang, H. Zhang, One-dimensional Fe2 P acts as a Fenton agent in response to NIR II light and ultrasound for deep tumor synergetic theranostics, Angew Chem. Int. Ed. Engl. 58 (8) (2019) 2407–2412, https://doi.org/10.1002/anie.201813702.
[7] K. Liang, H. Sun, Z. Yang, H. Yu, J. Shen, X. Wang, H. Chen, Breaking the redox homeostasis: an albumin-based multifunctional nanoagent for GSH depletion-assisted chemo-/chemodynamic combination therapy, Adv. Funct. Mater. (2021), https://doi.org/10.1002/adfm.202100355.
[8] Y. Wang, W. Yin, W. Ke, W. Chen, C. He, Z. Ge, Multifunctional polymeric micelles with amplified Fenton reaction for tumor ablation, Biomacromolecules 19 (6) (2018) 1990–1998, https://doi.org/10.1021/acs.biomac.7b01777.
[9] X. Zhong, X. Wang, L. Cheng, Y.a. Tang, G. Zhan, F. Gong, R. Zhang, J. Hu, Z. Liu, X. Yang, GSH-Depleted PtCu3 nanocages for chemodynamic- enhanced sonodynamic cancer therapy, Adv. Funct. Mater. 30 (4) (2019), https://doi.org/10.1002/adfm.201907954.
[10] W. Zhang, J. Lu, X. Gao, P. Li, W. Zhang, Y. Ma, H. Wang, B. Tang, Enhanced photodynamic therapy by reduced levels of intracellular glutathione obtained by employing a nano-MOF with Cu(II) as the active center, Angew Chem. Int. Ed. Engl. 57 (18) (2018) 4891–4896, https://doi.org/10.1002/anie.201710800.
[11] W.S. Yang, R. SriRamaratnam, M.E. Welsch, K. Shimada, R. Skouta, V.S. Viswanathan, J.H. Cheah, P.A. Clemons, A.F. Shamji, C.B. Clish, L.M. Brown, A.W. Girotti, V.W. Cornish, S.L. Schreiber, B.R. Stockwell, Regulation of ferroptotic cancer cell death by GPX4, Cell 156 (1–2) (2014) 317–331, https://doi.org/10.1016/j.cell.2013.12.010.
[12] L. Wang, Y. Liu, T. Du, H. Yang, L. Lei, M. Guo, H.F. Ding, J. Zhang, H. Wang, X. Chen, C. Yan, ATF3 promotes erastin-induced ferroptosis by suppressing system Xc(.), Cell Death Differ. 27 (2) (2020) 662–675, https://doi.org/10.1038/s41418-019-0380-z.
[13] Z. Dong, L. Feng, Y. Chao, Y. Hao, M. Chen, F. Gong, X. Han, R. Zhang, L. Cheng, Z. Liu, Amplification of tumor oxidative stresses with liposomal Fenton catalyst and glutathione inhibitor for enhanced cancer chemotherapy and radiotherapy, Nano Lett. 19 (2) (2019) 805–815, https://doi.org/10.1021/acs.nanolett.8b03905.
[14] Z. Dong, L. Feng, Y. Hao, Q. Li, M. Chen, Z. Yang, H. Zhao, Z. Liu, Synthesis of CaCO3-based nanomedicine for enhanced sonodynamic therapy via amplification of tumor oxidative stress, Inside Chem. 6 (6) (2020) 1391–1407, https://doi.org/10.1016/j.chempr.2020.02.020.
[15] A. Tagde, H. Singh, M.H. Kang, C.P. Reynolds, The glutathione synthesis inhibitor buthionine sulfoximine synergistically enhanced melphalan activity against preclinical models of multiple myeloma, Blood Cancer J. 4 (2014), e229, https://doi.org/10.1038/bcj.2014.45.
[16] X. Guo, Y. Cheng, X. Zhao, Y. Luo, J. Chen, W.E. Yuan, Advances in redox-responsive drug delivery systems of tumor microenvironment, J. Nanobiotechnol. 16 (1) (2018) 74, https://doi.org/10.1186/s12951-018-0398-2.
[17] H. Tang, C. Li, Y. Zhang, H. Zheng, Y. Cheng, J. Zhu, X. Chen, Z. Zhu, J.G. Piao, F. Li, Targeted Manganese doped silica nano GSH-cleaner for treatment of Liver Cancer by destroying the intracellular redox homeostasis, Theranostics 10 (21) (2020) 9865–9887, https://doi.org/10.7150/thno.46771.
[18] A.M. Vuckovic, R. Venerando, E. Tibaldi, V. Bosello Travain, A. Roveri, L. Bordin, G. Miotto, G. Cozza, S. Toppo, M. Maiorino, F. Ursini, Aerobic pyruvate metabolism

sensitizes cells to ferroptosis primed by GSH depletion, Free Radic. Biol. Med. 167 (2021) 45–53, https://doi.org/10.1016/j.freeradbiomed.2021.02.045.
[19] J. Chen, X. Wang, Y. Zhang, S. Zhang, H. Liu, J. Zhang, H. Feng, B. Li, X. Wu, Y. Gao, B. Yang, A redox-triggered C-centered free radicals nanogenerator for self-enhanced magnetic resonance imaging and chemodynamic therapy, Biomaterials 266 (2021), 120457, https://doi.org/10.1016/j.biomaterials.2020.120457.
[20] Q. Chen, X. Ma, L. Xie, W. Chen, Z. Xu, E. Song, X. Zhu, Y. Song, Iron-based nanoparticles for MR imaging-guided ferroptosis in combination with photodynamic therapy to enhance cancer treatment, Nanoscale 13 (9) (2021) 4855–4870, https://doi.org/10.1039/d0nr08757b.
[21] S. Dong, Y. Dong, T. Jia, S. Liu, J. Liu, D. Yang, F. He, S. Gai, P. Yang, J. Lin, GSH-depleted nanozymes with hyperthermia-enhanced dual enzyme-mimic activities for tumor nanocatalytic therapy, Adv. Mater. 32 (42) (2020), e2002439, https://doi.org/10.1002/adma.202002439.
[22] F. Gong, L. Cheng, N. Yang, O. Betzer, L. Feng, Q. Zhou, Y. Li, R. Chen, R. Popovtzer, Z. Liu, Ultrasmall oxygen-deficient bimetallic oxide MnWOX nanoparticles for depletion of endogenous GSH and enhanced sonodynamic cancer therapy, Adv. Mater. 31 (23) (2019), e1900730, https://doi.org/10.1002/adma.201900730.
[23] H. Sun, M. Feng, S. Chen, R. Wang, Y. Luo, B. Yin, J. Li, X. Wang, Near-infrared photothermal liposomal nanoantagonists for amplified cancer photodynamic therapy, J. Mater. Chem. B 8 (32) (2020) 7149–7159, https://doi.org/10.1039/d0tb01437k.
[24] Q. Jiang, M. Pan, J. Hu, J. Sun, L. Fan, Z. Zou, J. Wei, X. Yang, X. Liu, Regulation of redox balance using a biocompatible nanoplatform enhances phototherapy efficacy and suppresses tumor metastasis, Chem. Sci. 12 (1) (2020) 148–157, https://doi.org/10.1039/d0sc04983b.
[25] H. Hu, J. Chen, H. Yang, X. Huang, H. Wu, Y. Wu, F. Li, Y. Yi, C. Xiao, Y. Li, Y. Tang, Z. Li, B. Zhang, X. Yang, Potentiating photodynamic therapy of ICG-loaded nanoparticles by depleting GSH with PEITC, Nanoscale 11 (13) (2019) 6384–6393, https://doi.org/10.1039/c9nr01306g.
[26] S.J. Dixon, B.R. Stockwell, The hallmarks of ferroptosis, Annu. Rev. Cell Biol. 3 (1) (2019) 35–54, https://doi.org/10.1146/annurev-cancerbio-030518-055844.
[27] X. Meng, J. Deng, F. Liu, T. Guo, M. Liu, P. Dai, A. Fan, Z. Wang, Y. Zhao, Triggered all-active metal organic framework: ferroptosis machinery contributes to the apoptotic photodynamic antitumor therapy, Nano Lett. 19 (11) (2019) 7866–7876, https://doi.org/10.1021/acs.nanolett.9b02904.
[28] X. Guo, F. Liu, J. Deng, P. Dai, Y. Qin, Z. Li, B. Wang, A. Fan, Z. Wang, Y. Zhao, Electron-accepting micelles deplete reduced nicotinamide adenine dinucleotide phosphate and impair two antioxidant cascades for ferroptosis-induced tumor eradication, ACS Nano 14 (11) (2020) 14715–14730, https://doi.org/10.1021/acsnano.0c00764.
[29] K. Li, K. Xu, Y. He, L. Lu, Y. Mao, P. Gao, G. Liu, J. Wu, Y. Zhang, Y. Xiang, Z. Luo, K. Cai, Functionalized tumor-targeting nanosheets exhibiting Fe(II) overloading and GSH consumption for ferroptosis activation in liver tumor, Small (2021), e2102046, https://doi.org/10.1002/smll.202102046.
[30] Y. Xiong, C. Xiao, Z. Li, X. Yang, Engineering nanomedicine for glutathione depletion-augmented cancer therapy, Chem. Soc. Rev. 50 (10) (2021) 6013–6041, https://doi.org/10.1039/d0cs00718h.
[31] J.M. Brown, W.R. Wilson, Exploiting tumour hypoxia in cancer treatment, Nat. Rev. Cancer 4 (6) (2004) 437–447, https://doi.org/10.1038/nrc1367.
[32] H. Xiang, H. Lin, L. Yu, Y. Chen, Hypoxia-irrelevant photonic thermodynamic cancer nanomedicine, ACS Nano 13 (2) (2019) 2223–2235, https://doi.org/10.1021/acsnano.8b08910.
[33] B. Ouyang, F. Liu, S. Ruan, Y. Liu, H. Guo, Z. Cai, X. Yu, Z. Pang, S. Shen, Localized free radicals burst triggered by NIR-II light for augmented low-temperature photothermal therapy, ACS Appl. Mater. Interfaces 11 (42) (2019) 38555–38567, https://doi.org/10.1021/acsami.9b15009.
[34] J. Yang, R. Xie, L. Feng, B. Liu, R. Lv, C. Li, S. Gai, F. He, P. Yang, J. Lin, Hyperthermia and controllable free radical coenhanced synergistic therapy in hypoxia enabled by near-infrared-II light irradiation, ACS Nano 13 (11) (2019) 13144–13160, https://doi.org/10.1021/acsnano.9b05985.
[35] Y. Wan, G. Lu, J. Zhang, Z. Wang, X. Li, R. Chen, X. Cui, Z. Huang, Y. Xiao, J. Chelora, W. Zhang, Y. Liu, M. Li, H.Y. Xie, C.S. Lee, A biocompatible free radical nanogenerator with real-time monitoring capability for high performance sequential hypoxic tumor therapy, Adv. Funct. Mater. 29 (39) (2019), https://doi.org/10.1002/adfm.201903436.
[36] X. Li, Y. Liu, F. Fu, M. Cheng, Y. Liu, L. Yu, W. Wang, Y. Wan, Z. Yuan, Single NIR laser-activated multifunctional nanoparticles for cascaded photothermal and oxygen-independent photodynamic therapy, Nano-Micro Lett. 11 (1) (2019), https://doi.org/10.1007/s40820-019-0298-5.
[37] G. Huang, Y. Qiu, F. Yang, J. Xie, X. Chen, L. Wang, H. Yang, Magnetothermally triggered free-radical generation for deep-seated tumor treatment, Nano Lett. 21 (7) (2021) 2926–2931, https://doi.org/10.1021/acs.nanolett.1c00009.
[38] S. Jang, X.R. Chapa-Dubocq, Y.Y. Tyurina, C.M. St Croix, A.A. Kapralov, V.A. Tyurin, H. Bayir, V.E. Kagan, S. Javadov, Elucidating the contribution of mitochondrial glutathione to ferroptosis in cardiomyocytes, Redox Biol 45 (2021), 102021, https://doi.org/10.1016/j.redox.2021.102021.
[39] M. Sang, L. Han, R. Luo, W. Qu, F. Zheng, K. Zhang, F. Liu, J. Xue, W. Liu, F. Feng, CD44 targeted redox-triggered self-assembly with magnetic enhanced EPR effects for effective amplification of gambogic acid to treat triple-negative breast cancer, Biomater. Sci. 8 (1) (2019) 212–223, https://doi.org/10.1039/c9bm01171d.
[40] L.H. Wang, Y. Li, S.N. Yang, F.Y. Wang, Y. Hou, W. Cui, K. Chen, Q. Cao, S. Wang, T.Y. Zhang, Z.Z. Wang, W. Xiao, J.Y. Yang, C.F. Wu, Gambogic acid synergistically potentiates cisplatin-induced apoptosis in non-small-cell lung cancer through suppressing NF-kappaB and MAPK/HO-1 signalling, Br. J. Cancer 110 (2) (2014) 341–352, https://doi.org/10.1038/bjc.2013.752.
[41] D. Duan, B. Zhang, J. Yao, Y. Liu, J. Sun, C. Ge, S. Peng, J. Fang, Gambogic acid induces apoptosis in hepatocellular carcinoma SMMC-7721 cells by targeting cytosolic thioredoxin reductase, Free Radic. Biol. Med. 69 (2014) 15–25, https://doi.org/10.1016/j.freeradbiomed.2013.12.027.
[42] E. Hatami, M. Jaggi, S.C. Chauhan, M.M. Yallapu, Gambogic acid: a shining natural compound to nanomedicine for cancer therapeutics, Biochim. Biophys. Acta Rev. Canc (1) (2020), 188381, https://doi.org/10.1016/j.bbcan.2020.188381, 1874.
[43] M.K. Pandey, B. Sung, K.S. Ahn, A.B. Kunnumakkara, M.M. Chaturvedi, B.B. Aggarwal, Gambogic acid, a novel ligand for transferrin receptor, potentiates TNF-induced apoptosis through modulation of the nuclear factor-kappaB signaling pathway, Blood 110 (10) (2007) 3517–3525, https://doi.org/10.1182/blood-2007-03-079616.
[44] M.J. Seo, D.M. Lee, I.Y. Kim, D. Lee, M.K. Choi, J.Y. Lee, S.S. Park, S.Y. Jeong, E.K. Choi, K.S. Choi, Gambogic acid triggers vacuolization-associated cell death in cancer cells via disruption of thiol proteostasis, Cell Death Dis. 10 (3) (2019), 187, https://doi.org/10.1038/s41419-019-1360-4.
[45] L. Han, Y. Wang, X. Huang, F. Liu, C. Ma, F. Feng, J. Zhang, W. Liu, W. Qu, H. Pang, J. Xue, Specific-oxygen-supply functionalized core-shell nanoparticles for smart mutual-promotion between photodynamic therapy and gambogic acid-induced chemotherapy, Biomaterials 257 (2020), 120228, https://doi.org/10.1016/j.biomaterials.2020.120228.
[46] J.-S. Lan, L. Liu, R.-F. Zeng, Y.-H. Qin, J.-W. Hou, S.-S. Xie, S. Yue, J. Yang, R.J.Y. Ho, Y. Ding, T. Zhang, Tumor-specific carrier-free nanodrugs with GSH depletion and enhanced ROS generation for endogenous synergistic anti-tumor by a chemotherapy-photodynamic therapy, Chem. Eng. J. 407 (2021), https://doi.org/10.1016/j.cej.2020.127212.
[47] H.Z. Zhang, S. Kasibhatla, Y. Wang, J. Herich, J. Guastella, B. Tseng, J. Drewe, S.X. Cai, Discovery, characterization and SAR of gambogic acid as a potent apoptosis inducer by a HTS assay, Bioorg. Med. Chem. 12 (2) (2004) 309–317, https://doi.org/10.1016/j.bmc.2003.11.013.
[48] H. Liang, Z. Zhou, R. Luo, M. Sang, B. Liu, M. Sun, W. Qu, F. Feng, W. Liu, Tumor-specific activated photodynamic therapy with an oxidation-regulated strategy for enhancing anti-tumor efficacy, Theranostics 8 (18) (2018) 5059–5071, https://doi.org/10.7150/thno.28344.
[49] Y. Chao, L. Xu, C. Liang, L. Feng, J. Xu, Z. Dong, L. Tian, X. Yi, K. Yang, Z. Liu, Combined local immunostimulatory radioisotope therapy and systemic immune checkpoint blockade imparts potent antitumour responses, Nat. Biomed. Eng. 2 (8) (2018) 611–621, https://doi.org/10.1038/s41551-018-0262-6.
[50] H. Pan, C. Zhang, T. Wang, J. Chen, S.K. Sun, In situ fabrication of intelligent photothermal indocyanine green-alginate hydrogel for localized tumor ablation, ACS Appl. Mater. Interfaces 11 (3) (2019) 2782–2789, https://doi.org/10.1021/acsami.8b16517.
[51] Y. Xu, S. Zhao, Z. Weng, W. Zhang, X. Wan, T. Cui, J. Ye, L. Liao, X. Wang, Jelly-inspired injectable guided tissue regeneration strategy with shape auto-matched and dual-light-defined antibacterial/osteogenic pattern switch properties, ACS Appl. Mater. Interfaces 12 (49) (2020) 54497–54506, https://doi.org/10.1021/acsami.0c18070.
[52] K. Hayashi, W. Sakamoto, T. Yogo, Smart ferrofluid with quick gel transformation in tumors for MRI-guided local magnetic thermochemotherapy, Adv. Funct. Mater. 26 (11) (2016) 1708–1718, https://doi.org/10.1002/adfm.201504215.
[53] F. Abasalizadeh, S.V. Moghaddam, E. Alizadeh, E. Akbari, E. Kashani, S.M.B. Fazljou, M. Torbati, A. Akbarzadeh, Alginate-based hydrogels as drug delivery vehicles in cancer treatment and their applications in wound dressing and 3D bioprinting, J. Biol. Eng. 14 (2020) 8, https://doi.org/10.1186/s13036-020-0227-7.
[54] S. Brule, M. Levy, C. Wilhelm, D. Letourneur, F. Gazeau, C. Menager, C. Le Visage, Doxorubicin release triggered by alginate embedded magnetic nanoheaters: a combined therapy, Adv. Mater. 23 (6) (2011) 787–790, https://doi.org/10.1002/adma.201003763.
[55] Y. Hori, A.M. Winans, C.C. Huang, E.M. Horrigan, D.J. Irvine, Injectable dendritic cell-carrying alginate gels for immunization and immunotherapy, Biomaterials 29 (27) (2008) 3671–3682, https://doi.org/10.1016/j.biomaterials.2008.05.033.
[56] C. Zhang, G. Shi, J. Zhang, H. Song, J. Niu, S. Shi, P. Huang, Y. Wang, W. Wang, C. Li, D. Kong, Targeted antigen delivery to dendritic cell via functionalized alginate nanoparticles for cancer immunotherapy, J. Contr. Release 256 (2017) 170–181, https://doi.org/10.1016/j.jconrel.2017.04.020.
[57] X. Zhang, Y. Li, D. He, Z. Ma, K. Liu, K. Xue, H. Li, An effective strategy for preparing macroporous and self-healing bioactive hydrogels for cell delivery and wound healing, Chem. Eng. J. 425 (2021), https://doi.org/10.1016/j.cej.2021.130677.
[58] B. Ma, W. Dang, Z. Yang, J. Chang, C. Wu, MoS2 Nanoclusters-based biomaterials for disease- impaired wound therapy, Appl. Mater. Today 20 (2020), https://doi.org/10.1016/j.apmt.2020.100735.
[59] Y. Cao, W. Song, Q. Jiang, Y. Xu, S. Cai, S. Wang, W. Yang, Nanoparticles from ancient Ink endowing a green and effective strategy for cancer photothermal therapy in the second near-infrared window, ACS Omega 5 (11) (2020) 6177–6186, https://doi.org/10.1021/acsomega.0c00252.
[60] S. Wang, Y. Cao, Q. Zhang, H. Peng, L. Liang, Q. Li, S. Shen, A. Tuerdi, Y. Xu, S. Cai, W. Yang, New application of old material: Chinese traditional Ink for photothermal therapy of metastatic lymph nodes, ACS Omega 2 (8) (2017) 5170–5178, https://doi.org/10.1021/acsomega.7b00993.
[61] B.-Q. Chen, R.K. Kankala, Y. Zhang, S.-T. Xiang, H.-X. Tang, Q. Wang, D.-Y. Yang, S.-B. Wang, Y.S. Zhang, G. Liu, A.-Z. Chen, Gambogic acid augments black phosphorus quantum dots (BPQDs)-based synergistic chemo-photothermal therapy through downregulating heat shock protein expression, Chem. Eng. J. 390 (2020), https://doi.org/10.1016/j.cej.2020.124312.

[62] K.H. Yim, T.L. Prince, S. Qu, F. Bai, P.A. Jennings, J.N. Onuchic, E.A. Theodorakis, L. Neckers, Gambogic acid identifies an isoform-specific druggable pocket in the middle domain of Hsp90beta, Proc. Natl. Acad. Sci. U. S. A. 113 (33) (2016) E4801–E4809, https://doi.org/10.1073/pnas.1606655113.

[63] T. Sun, X. Chen, X. Wang, S. Liu, J. Liu, Z. Xie, Enhanced efficacy of photothermal therapy by combining a semiconducting polymer with an inhibitor of a heat shock protein, Mater. Chem. Front. 3 (1) (2019) 127–136, https://doi.org/10.1039/c8qm00459e.

[64] Y. Yang, W. Zhu, Z. Dong, Y. Chao, L. Xu, M. Chen, Z. Liu, 1D coordination polymer nanofibers for low-temperature photothermal therapy, Adv. Mater. 29 (40) (2017), https://doi.org/10.1002/adma.201703588.

[65] J. Sun, Y. Li, Y. Teng, S. Wang, J. Guo, C. Wang, NIR-controlled HSP90 inhibitor release from hollow mesoporous nanocarbon for synergistic tumor photothermal therapy guided by photoacoustic imaging, Nanoscale 12 (27) (2020) 14775–14787, https://doi.org/10.1039/d0nr02896g.

[66] P.E. Gisby, D.O. Hall, Biophotolytic H2 production using alginate-immobilized chloroplasts, enzymes and synthetic catalysts, Nature 287 (5779) (1980) 251–253, https://doi.org/10.1038/287251a0.

[67] X. Ling, X. Chen, I.A. Riddell, W. Tao, J. Wang, G. Hollett, S.J. Lippard, O.C. Farokhzad, J. Shi, J. Wu, Glutathione-scavenging poly(disulfide amide) nanoparticles for the effective delivery of Pt(IV) prodrugs and reversal of cisplatin resistance, Nano Lett. 18 (7) (2018) 4618–4625, https://doi.org/10.1021/acs.nanolett.8b01924.

[68] X. Chen, J. Li, R. Kang, D.J. Klionsky, D. Tang, Ferroptosis: machinery and regulation, Autophagy 17 (9) (2021) 2054–2081, https://doi.org/10.1080/15548627.2020.1810918.

[69] D. Tang, X. Chen, R. Kang, G. Kroemer, Ferroptosis: molecular mechanisms and health implications, Cell Res. 31 (2) (2021) 107–125, https://doi.org/10.1038/s41422-020-00441-1.

[70] Q. Jiang, K. Wang, X. Zhang, B. Ouyang, H. Liu, Z. Pang, W. Yang, Platelet membrane-camouflaged magnetic nanoparticles for ferroptosis-enhanced cancer immunotherapy, Small 16 (22) (2020), e2001704, https://doi.org/10.1002/smll.202001704.

[71] X. Wan, L. Song, W. Pan, H. Zhong, N. Li, B. Tang, Tumor-targeted cascade nanoreactor based on metal-organic frameworks for synergistic ferroptosis-starvation anticancer therapy, ACS Nano 14 (9) (2020) 11017–11028, https://doi.org/10.1021/acsnano.9b07789.

[72] S. Daum, M.S.V. Reshetnikov, M. Sisa, T. Dumych, M.D. Lootsik, R. Bilyy, E. Bila, C. Janko, C. Alexiou, M. Herrmann, L. Sellner, A. Mokhir, Lysosome-Targeting amplifiers of reactive oxygen species as anticancer prodrugs, Angew Chem. Int. Ed. Engl. 56 (49) (2017) 15545–15549, https://doi.org/10.1002/anie.201706585.

[73] L.S. Lin, T. Huang, J. Song, X.Y. Ou, Z. Wang, H. Deng, R. Tian, Y. Liu, J.F. Wang, Y. Liu, G. Yu, Z. Zhou, S. Wang, G. Niu, H.H. Yang, X. Chen, Synthesis of copper peroxide nanodots for H2O2 self-supplying chemodynamic therapy, J. Am. Chem. Soc. 141 (25) (2019) 9937–9945, https://doi.org/10.1021/jacs.9b03457.

[74] D. Li, Y. Li, The interaction between ferroptosis and lipid metabolism in cancer, Signal Transduct. Target Ther. 5 (1) (2020), 108, https://doi.org/10.1038/s41392-020-00216-5.

[75] W.S. Yang, K.J. Kim, M.M. Gaschler, M. Patel, M.S. Shchepinov, B.R. Stockwell, Peroxidation of polyunsaturated fatty acids by lipoxygenases drives ferroptosis, Proc. Natl. Acad. Sci. U. S. A. 113 (34) (2016) E4966–E4975, https://doi.org/10.1073/pnas.1603244113.

[76] W. Cui, D. Liu, W. Gu, B. Chu, Peroxisome-driven ether-linked phospholipids biosynthesis is essential for ferroptosis, Cell Death Differ. 28 (8) (2021) 2536–2551, https://doi.org/10.1038/s41418-021-00769-0.

[77] S. Shen, C. Zhu, D. Huo, M. Yang, J. Xue, Y. Xia, A hybrid nanomaterial for the controlled generation of free radicals and oxidative destruction of hypoxic cancer cells, Angew Chem. Int. Ed. Engl. 56 (30) (2017) 8801–8804, https://doi.org/10.1002/anie.201702898.

[78] X.Q. Wang, F. Gao, X.Z. Zhang, Initiator-loaded gold nanocages as a light-induced free-radical generator for cancer therapy, Angew Chem. Int. Ed. Engl. 56 (31) (2017) 9029–9033, https://doi.org/10.1002/anie.201703159.

[79] Z.H. Chen, Y. Saito, Y. Yoshida, E. Niki, Effect of oxygen concentration on free radical-induced cytotoxicity, Biosci. Biotechnol. Biochem. 72 (6) (2008) 1491–1497, https://doi.org/10.1271/bbb.80002.